



Beyond the ordinary acoustoelectric effect: Superluminal phenomena in the acoustic realm and phonon-mediated Bloch gain

A. Apostolakis ^{1,2,*}, A. G. Balanov ^{2,†}, F. V. Kusmartsev ^{2,3,4} and K. N. Alekseev ^{2,5}

¹*Institute of Physics, Czech Academy of Sciences, Na Slovance 2, CZ-18221, Prague, Czech Republic*

²*Department of Physics, Loughborough University, Loughborough LE11 3TU, United Kingdom*

³*College of Art and Science, Khalifa University, PO Box 127788, Abu Dhabi, United Arab Emirates*

⁴*Microsystem and Terahertz Research Center, Chengdu 610200, People's Republic of China*

⁵*Center for Physical Sciences and Technology, Vilnius LT-10257, Lithuania*



(Received 13 April 2022; revised 30 June 2022; accepted 5 July 2022; published 26 July 2022)

It has been shown that coherent phonons can be used as a potent tool for controlling and enhancing optoelectronic and transport properties of nanostructured materials. Recent studies revealed that interaction of acoustic phonons and fast-moving carriers in semiconductor heterostructures can be accompanied by electron-phonon instabilities that cause ordinary and induced Cherenkov effects. However, the development of such instabilities is still poorly understood. Our study shows that other supersonic phenomena, beyond the Cherenkov instability, are possible for nonequilibrium charge transport in the miniband semiconductor superlattices (SLs) driven by an acoustic plane wave. Using semiclassical nonperturbative methods and elements of the bifurcation theory, we find the conditions for the onset of dynamical instabilities (bifurcations) which are caused by the emission of specific SL phonons by supersonic electrons, and their back action on the electrons. Notably, the underlying radiation mechanism is connected either to normal or anomalous Doppler effects in full accordance with the Ginzburg-Frank-Tamm theory. The appearance of induced Doppler effects is also discussed in relation to the formation of electron bunches propagating through the spatially periodic structure of the SL. When the amplitude of the acoustic wave exceeds a certain threshold, the dynamical instabilities developed in the system are manifested as drift velocity reversals, resonances in sound attenuation, and absolute negative mobility. We demonstrate that the discovered superluminal Doppler phenomena can be utilized for tunable broadband amplification and generation of GHz-THz electromagnetic waves, which creates a ground for the development of novel phononic devices.

DOI: [10.1103/PhysRevB.106.014312](https://doi.org/10.1103/PhysRevB.106.014312)

I. INTRODUCTION

The mediating role of lattice vibrations (phonons) in nanocrystals has been readily recognized as a fundamental tenet in condensed matter physics. In particular, understanding in depth the transport properties of phonons and their interactions with electrons is important for enhancing the efficiency of thermoelectric nanostructures [1,2], developing acoustic metamaterials [3,4], or novel spectroscopic schemes [5,6]. In the past few years, there has been an intensive research aimed to study the connection between physics of coherent phonons excitation and nonequilibrium dynamics in electronic systems. Prominent examples include phononic devices based on two-dimensional (2D) materials [7–10] which can exhibit high electron mobility [9,10], high-frequency phonon transducers [11–13], and quantum structures where coherent acoustic phonons have been generated in the THz-GHz range [7,14–16]. Recently, there has been increased interest in amplification of acoustic phonons due to their interaction with fast moving carriers in semicon-

ductor superlattices (SLs) [16]. These experiments revealed the importance of electron-phonon instabilities where ordinary and induced Cherenkov effects come into play. In general, the Cherenkov effect is the well-known phenomenon encountered in the electrodynamics when a charged particle passes through a dielectric medium at speed greater than the phase velocity of light in the medium. We likewise note new research efforts devoted to the radiation dynamics of the superluminal particle [17–20]. Interesting examples include further developments in Ginzburg and Frank theory [21,22] describing the Doppler effects [20,23], Smith-Purcell radiation in plasmonic crystals [17], and nonperturbative generalization of Cherenkov radiation [19]. In the acoustic realm though, Cherenkov emission can be induced when the average electron velocity (v_d) in the presence of a static field moves faster than the speed of sound (v_s). This supersonic condition ($v_d > v_s$) is well satisfied in an electrically biased SL [16] where the propagating acoustic wave interacts with the electrically driven electron current. The aforementioned study further confirmed that Cherenkov effects and possibly other more exotic electromagnetic phenomena might have acoustic counterparts. It was only recently, when semiclassical studies and quantum-mechanical simulations [15,24,25] predicted that under the action of a strong acoustic wave, the

*Apostolakis@fzu.cz

†A.Balanov@lboro.ac.uk

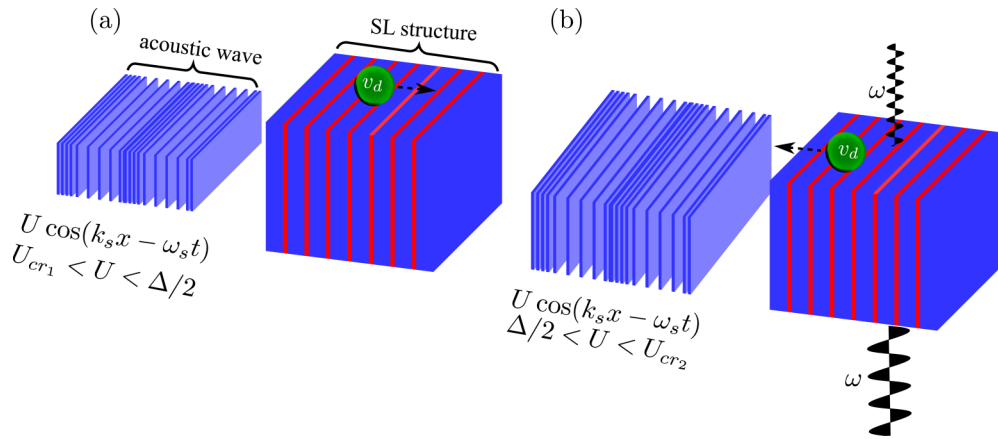


FIG. 1. Schematic diagram of novel electroacoustical effects beyond the ordinary charge drag. A strong acoustic plane wave of the energy amplitude U propagates at $v_s = \omega_s/k_s$ along the growth direction (x axis) of a superlattice (SL) with a miniband width of Δ and lattice period d . (a) For $U < \Delta/2$, charges are always transported along the direction of the wave propagation. However, bunches of electrons begin to oscillate strongly at $U = U_{cr_1}$, which is slightly below $\Delta/2$ [see Eq. (13)], and then drift of the bunches quickly slows down with an increase of U . (b) For $U > \Delta/2$, the electronic bunches move opposite to the propagating wave, and their backward drift becomes fastest at U_{cr_2} , which value is slightly above $\Delta/2$ [Eq. (13)]. Our analytical selection rules [Eq. (13)] indicate that the critical amplitudes U_{cr_1} and U_{cr_2} mark respectively superluminal anomalous and superluminal backward Doppler regimes [Eq. (16)] of emission and absorption of specific phonons [Eq. (13)] by the electrons. Additionally, at the wave amplitude U_{cr_2} , an interaction of the electrons with a high-frequency (ω) electromagnetic wave can result in its amplification.

propagating deformation potential can induce quasiperiodic Bloch oscillations of miniband electrons. The rise of these complex Bloch oscillations was linked to global instabilities triggered with an increase of the wave amplitude, which serves as control parameter [25]. Remarkably, the development of these instabilities clearly distinguishes the case of SL from the ordinary electroacoustic effect in bulk semiconductors with a quadratic band [26,27].

In this work, we study supersonic phenomena that should appear when a coherent acoustic stimulus induces high-frequency electron dynamics in semiconductor superlattice. In particular, we theoretically consider acoustically driven miniband electrons which tunnel through the SL periodic potential under the action of a longitudinal strain wave with energy amplitude U , as shown in Fig. 1(a). In this case, the acoustic stimulus interacts with the electrons by means of a deformation potential. We demonstrate that this interaction and the induced miniband transport are controlled by the laws of physics typical for superluminal particles with internal degrees of freedom [28]. In our case, the internal degrees of freedom are associated with the propagating strain-induced deformation potential. Analysis of the semiclassical phase space dynamics in the reference frame moving at v_s allowed to identify specific dynamical instabilities (bifurcations) which are developed for certain critical values of the strain-induced potential $U = U_{cr_n}$ ($n = 1, 2, \dots, U_{cr_1} < U_{cr_2} < \dots$). Tuning U to these values induces the formation of new bound states between the electrons and the phonons. We found out that the phonon-assisted transport involving those bound states are, in essence, a direct generalization of the normal and anomalous Doppler effects discussed in the radiation theories introduced by Ginzburg and Frank for supreluminal photons [22]. Our model parameters correspond to the regime related to the recently discovered superlight inverse Doppler effect [20]. Moreover, our results provide compelling arguments

for the long-standing idea introduced by Tamm [29] that the characteristics of the Ginzburg-Frank radiation theory can be implemented to supersonic acoustical systems. The emitted phonons which are involved in the radiation processes are found to behave in a manner similar to a Smith-Purcell (SP) photons [30,31].

Our study showed that stimulated emission creates electron bunches which move along the spatially periodic structure of the SL. For both normal and anomalous Doppler behaviors, the electron bunching effects on directed charge transport appear to be robust even when we take into account scattering processes. Remarkably, the involvement of the anomalous Doppler effects for $U < \Delta/2$ decelerates the single electron with the overall drift velocity remaining positive. Here Δ is the first miniband width, within which a charge tunneling transport is assumed. For $U > \Delta/2$, the reversal of the drift results from the emergence of both anomalous and conventional normal Doppler shifts.

Signatures of the Doppler effects are also found in attenuation of the acoustic wave, which is characterized by the calculated absorption coefficient. We also demonstrate a possibility of absolute negative mobility (ANM) for a SL structure in combined dc bias and acoustic wave drive with sufficient large amplitude to induce superluminal Doppler effects. Notably, ANM has already attracted great research interest in connection to spontaneous generation of large static fields [32] and high-frequency stimulated emission of photons [33] when the superlattice structure is driven by intense terahertz electric fields.

Our analysis shows that the discovered phenomena can be exploited practically in schemes for tunable broadband amplification and generation of GHz-THz electromagnetic waves. Note that SLs under moderate electric fields have been already shown as a system to provide optical gain due to the Bloch oscillations in the presence of weak dissipation [34,35]. This

prediction was based on semiclassical arguments and coined as Bloch gain, raising the possibility of inversionless lasing in a dc biased SL. The use of phononic waves though, opens new opportunities to enhance the performance of superlattice oscillators. Here we put forward a scheme for the broadband amplification of THz radiation in acoustically driven superlattice similar to the Bloch gain in a electrically biased SL.

This paper is organized as follows. In Sec. II, we employ elements of the bifurcation theory and we consider the conditions for which the superluminal nature of electron kinematics arises. Therefore we identify a class of Cherenkov and Doppler resonances which are directly connected to global bifurcations developing with an increase of the wave amplitude. In Sec. III, we discuss electron bunching and the related induced Doppler effects for choices of the wave amplitude between the analytical bifurcations points which is confirmed by numerical calculations determining the kinetic behavior of a classical ensemble of particles. In Sec. IV, a non-perturbative solution of the Boltzmann transport equation is followed to examine the main transport characteristics in SL at the presence of scattering. We discuss the feasibility of ANM, for an electrically biased SL in Sec. V and the broadband amplification of an electromagnetic (EM) wave for an acoustically pumped SL in Sec. VI. We conclude in Sec. VII with a few remarks.

II. SUPERLUMINAL PHENOMENA IN THE REALM OF ACOUSTOELECTRIC INTERACTIONS

This section discusses the nature of the acoustoelectric effects in SLs. The nonlinear analysis of the acoustoelectric instabilities provides a fruitful insight for the absorption of the acoustic wave, its scattering by miniband electrons and the related quantum processes. This would allow us to show that a wide range of superluminal phenomena have distinct acoustic counterparts.

We consider a longitudinal acoustic wave that propagates in the direction of the superlattice axis (x) [Fig. 1(a)] generating a position and time-dependent potential energy given by [24,36]

$$V(x, t) = -U \sin[(k_s(x + x_i) - \omega_s t)], \quad (1)$$

where $U = D\epsilon$ is defined by the deformation potential constant D and the strain magnitude ϵ . The displacement x_i defines the initial phase of the driving wave, ω_s is the wave frequency, v_s is the speed of sound in the materials of SL, $k_s = \omega_s/v_s$ is the wave number, and t is time. In the simplest tight-binding scheme, it sufficient to describe the dispersion of the first SL miniband as [37]

$$\mathcal{E}(p_x) = \frac{\Delta}{2} \left[1 - \cos\left(\frac{p_x d}{\hbar}\right) \right], \quad (2)$$

where \mathcal{E} is the energy of an electron with quasimomentum p_x , Δ is the miniband width, and d is the SL period. In general, the dispersion relation should also include a contribution of the lateral (along the superlattice layers) motion in the form $\mathcal{E}_{\parallel}(p_y, p_z) = p_y^2/2m^* + p_z^2/2m^*$, where m^* is the effective electron mass. However, without account of anisotropic scattering the electron motion in lateral directions is independent from electron tunneling along the superlattice axis,

TABLE I. Basic parameters of superlattices studied. The frequency of sound is assumed $\omega_s = 4 \times 10^{11}$ rad/s with $\omega_s \sim 0.1/\tau$ and $k_s \sim 1/d$, unless stated otherwise. Further details are given in Appendix E.

Δ (meV) miniband width	d (nm) lattice period	τ (fs) scattering time	v_s (m/s) velocity of sound	D (eV) Deformation potential
7	12.5	250	5000	10
20	11.4			

and therefore the most interesting physical effects can be described by the semiclassical Hamiltonian

$$H(x, p_x) = \mathcal{E}(p_x) + V(x, t). \quad (3)$$

It is easy to see from this Hamiltonian, the electron velocity, $\partial\mathcal{E}/\partial p_x$ and the force acting on the electrons, $-\partial H/\partial x$, due to the propagating deformation potential Eq. (1), which read respectively

$$v = \frac{\partial\mathcal{E}}{\partial p_x} = v_0 \sin\left(\frac{p_x d}{\hbar}\right), \quad (4a)$$

$$\frac{dp_x}{dt} = -\frac{\partial H}{\partial x} = k_s U \cos[(k_s(x + x_i) - \omega_s t)], \quad (4b)$$

with $v_0 = \Delta d/(2\hbar)$ being the maximal miniband velocity. It has been demonstrated that this simple model well describes the experiments on charge transport in SL driven by a train of picosecond strain pulses [12,15]. We consider mainly two different sets of parameters which are summarized in Table I corresponding to GaAs/Al_xGa_{1-x}As SLs used in recent experiments [16,38]. Our model Eq. (4) though has comfortably allowed us to calculate similar results for a wide range of SL parameters.

Efficient interaction of electrons with phonons. We turn now to the condition for efficient interaction of the band electrons with acoustic phonons that was initially introduced in the theory of ultrasound absorption in metals. In the case, the mean free path of electrons is large, the absorption of the sound wave can be considered as scattering of an aggregate of phonons by those electrons whose velocity in the direction of the acoustical wave vector is equal to the phase velocity of sound [39,40]. Indeed, for $v > v_s$, the conservation laws should dictate that for the absorption of a phonon

$$p_f = p_i + \hbar q, \quad (5a)$$

$$\mathcal{E}(p_f) = \mathcal{E}(p_i) + \hbar\omega_q, \quad (5b)$$

where p_f (p_i) stands for the final (initial) momentum of the electron, and $\hbar q > 0$ is the quasimomentum of the absorbed phonon. For generality, we assume here that the phonon frequency ω_q can be different from the frequency of the propagating deformation potential (1). Combining Eqs. (5a) and (5b) we obtain $\mathcal{E}(p_i + \hbar q) = \mathcal{E}(p_i) + \hbar\omega_q$. Since the momentum exchanged between the low-frequency phonons and band electrons is very small, $\hbar q \ll p_i$, the energy then $\mathcal{E}(p_i + \hbar q)$ can be expanded into Taylor series as

$$\mathcal{E}(p_f) \approx \mathcal{E}(p_i) + \hbar v(p_f)q. \quad (6)$$

By comparing Eqs. (6) and (5b), we have

$$v \approx v_s = \omega_q/q, \quad (7)$$

which corresponds to Cherenkov effect [39,41,42]. It can be shown that the same condition Eq. (7) needs to be satisfied in order an electron emits a phonon with a small quasimomentum $\hbar q$. In this derivation, it was implicitly assumed that influence of the electron potential energy in scattering events is negligible, and also that the electrons oscillate far from edges of the first Brillouin zone. Now we are going to show that the resonant condition Eq. (7) naturally arises in the analysis of the fixed points of the dynamical system Eq. (3).

Fixed points and their physical meaning. We first make a canonic transformation to the moving with the velocity v_s reference frame, for which new Hamiltonian, electron kinetic energy and coordinate take the forms

$$H' = \mathcal{E}'(p_x) + V(x'), \quad \mathcal{E}'(p_x) = \mathcal{E}(p_x) - v_s p_x, \\ x'(t) = x(t) + x_0 - v_s t,$$

where the expressions for $V(x)$ and $\mathcal{E}(p_x)$ are still given by Eqs. (1) and (2). While the Hamiltonian H' becomes time-independent, the electron momentum p_x is unchanged under the canonic transformation. In Appendix A, we showed that the fixed points of this autonomous dynamic system are

$$x' = \frac{\pi}{2k_s} + \frac{m\pi}{k_s}, \quad (8a)$$

$$p_x = (-1)^l \frac{\hbar}{d} \sin^{-1} \left(\frac{v_s}{v_0} \right) + l \frac{\hbar\pi}{d}, \quad (8b)$$

where m and l are arbitrary integer numbers.

To understand physical meaning of the fixed points we first consider the case of small U when $p_x(t)$ oscillations are well confined within the first Brillouin zone $|p_x d/\hbar| < \pi$, evoking thereby only the conventional acoustoelectric response. Importantly, Eq. (8b) for the p components originates from the condition $v(p_x) = v_s$ [cf. Eq. (A3a)], which is identical to Eq. (7). Therefore Cherenkov absorption or emission of phonons can arise in the proximity of the stationary points. Figure 2 demonstrates schematically the modulus of electron velocity in the momentum subspace and the positions therein of the hyperbolic points (red circles): $p_{s1} = (\hbar/d) \sin^{-1}(v_s/v_0)$, $p_{s2} = \pi d/\hbar - (\hbar/d) \sin^{-1}(v_s/v_0)$, and $p_{s3} = -\pi \hbar/d - (\hbar/d) \sin^{-1}(v_s/v_0)$, which are connected by a horizontal line corresponding to the condition [see Eq. (7)] for the direct absorption of phonons by electrons. More detailed consideration shows that both forward and backward Cherenkov [42,43] effects can exist for supersonic miniband electrons. For extended discussion see Appendix A.

The back action of such Cherenkov phonons on the miniband electrons is definitely small. In what follows, we will discuss an opposite situation of significant changes in the transport of the miniband electrons caused by their interactions with such phonons that are able to carry large momenta and therefore able to exert energy transitions both in the miniband Eq. (2) and in the potential wells formed by the acoustic wave Eq. (1). Of course, this will require relatively large amplitudes of the wave $U \gtrsim \Delta/2$, when effects of the electron potential energy cannot be ignored any more.

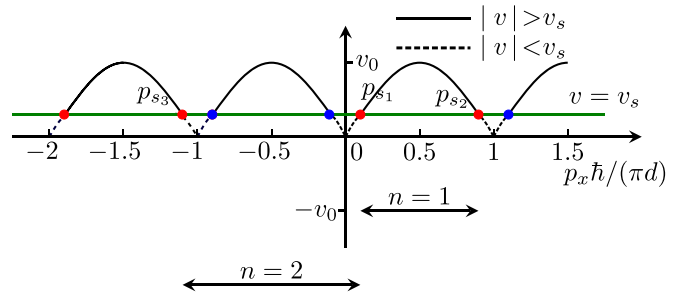


FIG. 2. The modulus of electron velocity $|v(p_x)|$ [Eq. (4a)] represented by dashed lines corresponding to subsonic charge carriers and solid curves to supersonic electrons that belong to the active zone and therefore they can emit or absorb phonons while making transitions within the miniband. The green horizontal line connects the hyperbolic points p_{s_i} [Eq. (7)], with $i = 1, 2$, and 3 , denoting the condition for absorption of the acoustic wave for small U [see Eq. (8)]. The arrows ($n = 1$) and ($n = 2$) indicate which hyperbolic points are connected in order to satisfy the selection rules described by Eq. (13).

The emergence of Doppler effects. Next, we will reveal superluminal mechanisms and the related instabilities (bifurcations) that are developed for larger U . A series of global bifurcations with the increase of U have been analytically found previously for the model described by Eq. (4) [25]. It has been shown that they are associated with the reconnection of the hyperbolic points [see Eq. (8)] by separatrices in the phase space of the dynamical system Eq. (A2) at the following critical values of U :

$$U_{\text{cr}_n} = \frac{\Delta}{2} \sqrt{1 - \left(\frac{v_s}{v_0} \right)^2} + \frac{\hbar v_s q_n}{2} \quad (n \geq 1), \quad (9a)$$

$$q_n = \frac{2}{d} \sin^{-1} \left(\frac{v_s}{v_0} \right) + (2n - 3) \frac{\pi}{d}, \quad (9b)$$

where n is an integer designating the order of the bifurcation. From physical point of view, Eqs. (9) imply multiphonon resonances in a transition scattering of the sound wave by electrons [44] placed in the SL periodic potential. Specifically, the second term in Eq. (9a) defines an acoustic phonon quantum $\hbar\omega(q_n) = \hbar v_s q_n$ with the effective wave number q_n Eq. (9b), while the first term in Eq. (9a) is proportional to the width of the active zone in energy band, which will be discussed later. The emission and absorption of phonons with wavenumber q_n [Eq. (9b)], however, at critical (bifurcation) points result in both normal ($n = 1$) and Umklapp ($n \geq 2$) scattering transitions of electrons in momentum space. As can be seen in Fig. 2, the two hyperbolic points (p_{s1}, p_{s2}) which are involved in the first bifurcation (Fig. 13) with critical value

$$U_{\text{cr}_1} = \frac{\Delta}{2} \frac{[\cos(p_{s1} d/\hbar) - \cos(p_{s2} d/\hbar)] + v_s p_{s1} - v_s p_{s2}}{\sin(k_s x_{s2}) - \sin(k_s x_{s1})}, \quad (10)$$

lie within the first BZ resulting in an electron normal scattering transition in p_x space. In contrast, an electron Umklapp scattering stems from the second bifurcation with critical

value

$$U_{\text{cr}2} = \frac{\frac{\Delta}{2} [\cos(p_{s_2}d/\hbar) - \cos(p_{s_3}d/\hbar)] + v_s p_{s_2} - v_s p_{s_3}}{\sin(k_s x_{s_3}) - \sin(k_s x_{s_2})}, \quad (11)$$

in which the separatrix is reconnected (see Fig. 14) through (p_{s_1}, p_{s_3}) with p_{s_3} being located outside the first BZ. Note that Eqs. (9) for $n = 1, 2$ can be derived from Eqs. (10) and (11), respectively, by just rearranging their terms.

The active zone region. The stationary points of hyperbolic type (x_s, p_s) define intervals of supersonic electron motion in the momentum subspace p_x . Within these intervals the momentary electron velocity $v(p_x)$ can exceed the sound velocity v_s . In detail, the pairs of resonant points (p_{s_1}, p_{s_2}) and (p_{s_1}, p_{s_3}) determine intervals within the first Brillouin zone, $0 < p_x < \pi\hbar/d$ and $-\pi\hbar/d < p_x < 0$ respectively, in which the supersonic motion (with the velocity in Fig. 2 represented by black solid lines) takes place. It follows that $v(p_x) > v_s$ holds for an energy interval that is centered at the middle of the energy band $\mathcal{E} = \Delta/2$, and has the width

$$\delta\mathcal{E}_{v>v_s} = \Delta \left[1 - \left(\frac{v_s}{v_0} \right)^2 \right]^{1/2}. \quad (12)$$

Supersonic electrons belonging to the ‘‘active zone’’ defined by Eq. (12) can emit phonons while following the phase trajectories defined by Eq. (A5). When the maximal miniband velocity v_0 is approaching the speed of sound v_s , the active zone becomes narrow $\delta\mathcal{E}_{v>v_s} \rightarrow 0$.

Hypersonic limit. We now consider the implications of the opposite limit $v_0/v_s \gg 1$, which is well satisfied for typical semiconductor SLs (see Table II in Appendix E) and where the superluminal physics become more transparent. In this case, the active zone practically coincides with the entire miniband, $\delta\mathcal{E}_{v>v_s} \rightarrow \Delta$ and therefore practically eliminating the subsonic regions (black dashed lines) between blue and red circles in Fig. 2; see discussion in Appendix E. Physically, it guarantees that the miniband electron speed $v = v_0 |\sin(p_x d/\hbar)|$ exceeds the speed of sound v_s almost for any momentum p_x . Additionally, the hyperbolic points Eq. (8b), involved in the derivation of Eq. (9), are located at $p_s \approx 0$ and very close to the boundaries of the first and successive BZs. In what follows, we will mainly focus on the first two major bifurcations, for which

$$U_{\text{cr}1,2} = \frac{\Delta}{2} \mp \frac{\hbar\omega_q}{2}, \quad \omega_q = \pi v_s/d, \quad (13)$$

since their effects play a fundamental role, as we will see, in the electron kinetics. It is easy to see that the relative contribution of the terms $\Delta/2$ and $\hbar\omega_q/2$ to the value U_{cr} in Eq. (13) is defined by the ratio v_0/v_s . Therefore, in the physically interesting limit $v_0/v_s \gg 1$ the critical wave amplitude U_{cr} asymptotically approaches the value $U_0 = \Delta/2$, i.e., the half of the miniband width. The limit $v_0/v_s \rightarrow \infty$ itself can be reached either by increasing Δ , or by slowing down the speed of sound $v_s \rightarrow 0$. The later demonstrates that the appearance of the quantum in criterion Eq. (13) is directly related to the propagation effects.

To get a deeper insight into the physical meaning of Eq. (13), consider an electron that absorbs or emits a phonon with the quasimomentum $\hbar q = \hbar 2\pi/\lambda_q = h/2d$. As a result

of the radiation/absorption act, the electron momentum becomes $p_f = p_i + \hbar q$, where p_f (p_i) stands for the final (initial) momentum and q is positive or negative depended on whether we have absorption or emission processes. Next, a variation of the electron kinetic energy in the moving reference frame of the acoustic wave is

$$\delta\mathcal{E}' = \delta\mathcal{E} - v_s \delta p, \quad (14)$$

where $\delta\mathcal{E} = \mathcal{E}(p_f) - \mathcal{E}(p_i)$ and $\delta p = p_f - p_i$. Assuming the electron is initially at the center of Brillouin zone $p_i = 0$, it is easy to find both the variation of the electron kinetic energy $\delta\mathcal{E} = \Delta$ and the variation of its momentum $\delta p = \hbar\omega_q/v_s$. Finally, equating $\delta\mathcal{E}'$ to the corresponding variation of the electron potential energy $\delta V = V_f - V_i$, we get the condition of energy conservation in the moving frame as

$$\delta V = -\Delta \pm \hbar\omega_q. \quad (15)$$

Now consider an electron transition from the top of the potential $V(x')$ at $x'_s = -\pi/(2k_s)$ to its bottom at $x'_s = \pi/(2k_s)$, for which $\delta V = -U - (+U) = -2U$. Substituting this δV in Eq. (15) we obtain Eq. (13). Therefore the values of the critical amplitudes $U_{\text{cr}1,2}$ follow from a delicate energy balance in distribution of the acoustic wave energy ($2U$) between an excitation of the electron within the miniband ($\mathcal{E}_0 = 0 \rightarrow \mathcal{E}_f = \Delta$) and absorption or emission of the quantum $\hbar\omega_q$. Since we have assumed that $p_i = 0$ (lattice temperature close to zero), the first bifurcation is related to an absorption process in order to satisfy simultaneously Eqs. (13)–(15). On the other hand, the same initial condition results in emission of a phonon after the second bifurcation. While the energy of the quantum is relatively small $\hbar\omega_q/\Delta \ll 1$, it brings a large momentum inversely proportional to the lattice period d [see Eq. (9b) for $n = 1$]. Thereby this inelastic scattering event is able to kick the electron from the bottom of the miniband directly to its upper edge, giving rise to the electron Bragg reflections. The condition of energy conservation Eq. (15) in the moving frame can be rewritten in the alternative form

$$-\hbar\omega_0 = \hbar(-q|v_e| \pm \omega_q), \quad (16)$$

where $|v_e| = 2v_0/\pi$ is the effective electron speed and $\omega_0 = |\delta V|/\hbar$ is the resonant frequency which corresponds to the source excitation energy δV .

Remarkably, Eq. (16) describes both the normal and anomalous Doppler effects, depending on the sign in from of ω_q . Namely, entrance of $+\omega_q$ corresponds to anomalous Doppler effect, while $-\omega_q$ implies a normal Doppler effect.

In our system, the first resonance (at $U = U_{\text{cr}1}$) is associated with the anomalous Doppler effect. The anomalous character of the process is reflected in the fact that despite an electron absorbs the phonon $\hbar\omega_q$ (red wavy arrow), it makes transition from the top of the potential to its bottom (red vertical arrow) as illustrated in the left panel of Fig. 3(a). Thus the absorption of a quantum happens at the expense of potential energy, whereas the electron is excited at the upper edge of the miniband as indicated by the red arrow in the right panel of Fig. 3(a). Note that the SL parameters considered in this work can also operate in the regime where new phenomena such as the superlight inverse Doppler effect [20] are possible and thus $|\delta V| > \hbar\omega_q$ whereas the corresponding Doppler frequency shift has $\Delta\omega = \omega_q - \omega_0 < 0$. Regardless of the

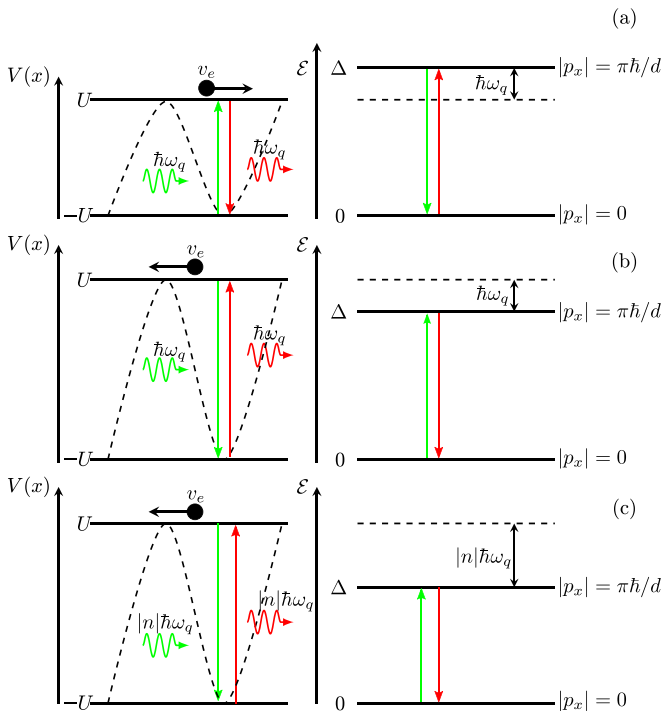


FIG. 3. Diagrams of electron transitions within the potential of the acoustic wave (left) and within the energy miniband (right) manifested by anomalous and normal Doppler effects corresponding to the bifurcations in increasing order. (a) The electron trapped by the wave $V(x)$ can either absorb the phonon $\hbar\omega_q$ and make a transition from the top of the potential $V_{\min} = U$ to its bottom $V_{\max} = -U$ or follow the reverse process by emitting a quantum. (b) The electron recoils, while emitting a phonon, leading to a normal Doppler shift of the transition (green arrow). Alternatively, the electron experiences an excitation (red arrow) assisted by absorption of $\hbar\omega_q$. (c) One-step multiphonon transitions involving odd number of normal Doppler shifts. The green lines describe emission processes where the red lines absorption ones.

anomalous radiation act, just after the first bifurcation the miniband electron (black circle with the right-handed arrow) continues to move in the positive direction with effective particle velocity, v_e . For detailed discussion of electron's kinetic behavior see the following Secs. III and IV. In similar way, one could also analyze the radiating processes far from the thermal equilibrium (at high temperature limit) by considering that the electron could initially sit at the edge of Brillouin zone ($p_i = \pi\hbar/d$) and subsequently inelastically scattered to center of the first Brillouin zone at $p_i = 0$. This process is depicted by the green vertical arrows of Fig. 3(a). On these terms, the anomalous character of the process would lie in electron emitting the phonon $\hbar\omega_q$ (green wavy arrow) and making a transition from the bottom of the potential to its top. Here, the emission of a quantum would happen instead at the expense of the kinetic energy. In this sense our model can accommodate a further generalization of the Ginsburg-Frank-Tamm theory [29].

After the second bifurcation (at $U = U_{\text{cr}_2}$), which corresponds to a normal Doppler effect, the realization of electronic transition from the top to the bottom of the potential [green arrow, left panel Fig. 3(b)] is conventionally accompanied

by an emission of a phonon. That, however, makes the electron to be excited [green arrow, right panel Fig. 3(b)] within the miniband. Notably, such a transition can be associated with the backward Cherenkov radiation [23,43], where the electron (black circle with left-handed arrow) moves in the opposite direction with respect to the emitted phonon and the associated Doppler-type frequency shift has $\Delta\omega < 0$. On the contrary, for an arbitrary system such as Larmor oscillator [45], the conventional normal Doppler effect holds $\omega_0 = \omega_q - q|v_e|$ with $\Delta\omega > 0$. The appearance of the Cherenkov effect in periodic photonic structures has demonstrated inherit connections between electron-photon interactions manifested by the Smith-Purcell effect and the Cherenkov effect [46]. Similarly, here is the SL which can play a role of an effective diffraction grating for Smith-Purcell-type phonons. We can identify that resonances Eq. (13) describe the SP mechanism where the emission spectrum is determined only by the period of the SL sample ($\omega_q \propto 1/d$) which constitutes an effective diffraction grating. The emitted radiation at wave number q (cf. Eq. (2) in Ref. [31]) taken in the limits $\beta = v/v_s \gg 1$ is reduced to a form containing the characteristic Doppler factor so that the angle of emission is either $\theta = 0$ or $\theta = \pi$. Finally, it is possible to examine the phonon absorption (emission) processes for higher order bifurcations at U_{cr_n} , $n \geq 3$, see Eq. (9a). For example, a three-phonon process can occur if the electron is inelastically scattered by a strong sound wave (at $U = U_{\text{cr}_3}$) which allows to perform a radiating transition from the bottom to the top of the miniband [see the right panel of Fig. 3(c)]. This higher-order process involves stimulated events which are illustrated by the vertical arrows in the left panel of Fig. 3(c) and they are facilitated on the boundaries of the first and the third Brillouin zone. Thus we obtain an realization of Umklapp processes which result in the inelastic scattering of electron back into the regime of normal Doppler effect.

III. ELECTRON BUNCHES AND INDUCED DOPPLER EFFECTS

In this section, we discuss the role of the induced Doppler effects in nonlinear mechanisms, similar to laser-plasma interactions [28,47] and relativistic microwave devices [48], leading to formation of traveling electron bunches. In the presence of a small-amplitude acoustic wave some of the electrons are captured by the propagating potential, forming a group of trapped electrons (electron bunch) and perform oscillatory motion within potential itself. However, if the acoustic stimuli are strong enough they can enforce the electrons to perform complex Bloch oscillations (phonon-assisted trajectories) [24,25], which, as we found out, causes the electron bunches to oscillate with large amplitude in p_x space. To understand the role of these effects in the acoustically driven charge transport in SL we analyze the solution of the Boltzmann transport equation (BTE)

$$\frac{\partial f}{\partial t} + v(p_x) \frac{\partial f}{\partial x} + eE(x, t) \frac{\partial f}{\partial p} = \text{St}[f], \quad (17)$$

where $\text{St}[f]$ is the collision term specified later, $f(x, p_x, t)$ is the electron distribution function, $E(x, t) = E_s \cos(k_s x - \omega_s t)$ is a force field derived from the potential energy function

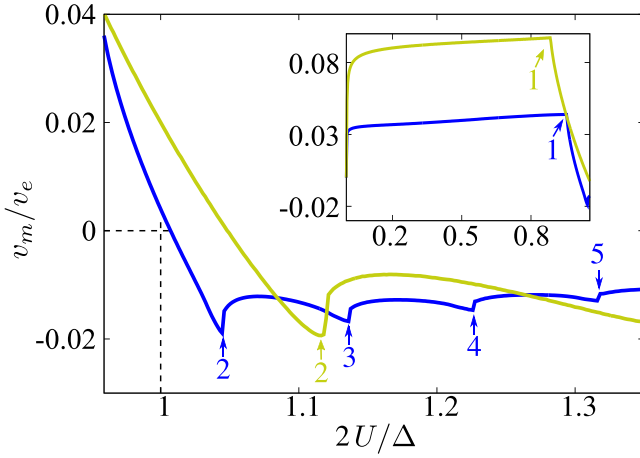


FIG. 4. The velocity v_m of the electron bunches as a function of the wave amplitude U in the quasiballistic regime for $v_e/v_s = 22$ (blue curve) and 10.5 (yellow curve); See Table II. The dashed line at $U_0 = \Delta/2$ separates the forward motion of the electron bunches from the backward one with respect to the propagation of acoustic wave for $v_e/v_s \rightarrow \infty$. The comparison with the superluminal selection rules [Eq. (18)] is indicated by the arrows. The inset shows the full development of v_m with an increase of U around the first selection rule (anomalous Doppler condition). The acoustic wave in both cases has a frequency lying at $\omega_s = v_s/d$ with d the lattice period of each SL structure.

$V(x, t)$ with $E_s = k_s U/e$ denoting the amplitude of the effective acoustoelectric field.

We first consider the quasiballistic regime $a = k_s l \gg 1$, where $l = v_0 \tau$. Here l denotes the mean free path of the carriers being sufficiently larger than the sound wavelength and τ is the electron scattering time. In this case, the collision term in Eq. (17) can be neglected as $\text{St}[f] \rightarrow 0$. In addition, the value of the sound frequency considered in our calculations is, $\omega_s = 4 \times 10^{11}$ rad/s with $k_s \sim 1/d$, which lies far away from the frequency ranges of the phonon stop bands [49,50]. To characterize the kinetic properties the electrons bunches, we introduce the average momentum $p_a = p_\phi \hbar/d$, where $p_\phi = \arg(m_1)$ is a circular mean angle. Here $m_1 = \langle \exp(ip_x(t)d/\hbar) \rangle_{x_i}$ is the first trigonometric moment m_1 of the distribution function [51,52]. The operator $\langle \cdot \rangle_{x_i}$ performs averaging over an ensemble of time-dependent electron trajectories starting with the same initial momentum $p_i = 0$ (low temperature limit) and different initial positions $x_i \in [-\lambda/2, \lambda/2)$, where $\lambda = 2\pi/k_s$ means the acoustic wave length.

Figure 4 presents the dependencies of the time-averaged electron velocity $v_m = \langle v_0 \sin(p_a(t)d/\hbar) \rangle_{\Delta t}$ on the wave amplitude U which are numerically calculated (see Appendix B for more details) for two different ratios v_e/v_s . Both graphs demonstrate series of local minima of v_m , which are reached at the critical values of $U = U_{\text{cr}_n}$. By rearranging terms, Eq. (13) can be rewritten in the form

$$U_{\text{cr}_n} = \frac{\Delta}{2} \left[1 + (2n-3) \frac{v_s}{v_e} \right], \quad (18)$$

which, as it was mentioned above, in the limit $v_e/v_s \rightarrow \infty$ reveals a localization condition

$$U_{\text{cr}_n} \rightarrow U_0 = \frac{\Delta}{2}. \quad (19)$$

These values are highlighted by arrows with the numbers indicating the index n in Eq. (18), while the dashed line at $U_0 = \Delta/2$ separates the forward motion of the electron bunches from the backward one with respect to the propagation of acoustic wave for $v_e/v_s \rightarrow \infty$. The graphs evidences that for larger v_e/v_s , the U -value corresponding to reversing of the electron velocity v_e comes closer to U_0 , thus confirming the localization criterion Eq. (19).

The Doppler effects as described in the previous section are elementary processes whereas here the induced Doppler effects correspond to collective processes triggered by an instability in which an elementary radiation act can induce sequentially another one. This becomes more evident, as we shall see, by the behavior of the electron dynamics between the bifurcations. Figure 5(a) shows the temporal dynamics of the electron distribution function by solving Eq. (17) for $U < U_{\text{cr}_1}$, while Fig. 5(b) for the case $U_{\text{cr}_1} < U < U_0$. The color in (a) and (b) relates to the values of reduced electron distribution function $\tilde{f}(p_x, t) = 1/\lambda \int_{-\lambda/2}^{\lambda/2} f(x, p_x, t) dx$, where it changes from black for the lowest value to red—for the highest one which indicates the presence of an enhanced concentration of electron trajectories (electron bunches) around the center of Brillouin zone. As U increases beyond U_{cr_1} , the electron dynamics become more complicated which is manifested in appearance of quite sophisticated patterns in $\tilde{f}(p_x, t)$, compare Fig. 5(a) for the case of $U < U_{\text{cr}_1}$ and Fig. 5(b) for the case of $U > U_{\text{cr}_1}$. While the former figure demonstrate rather regular pattern, the latter shows signatures of turbulent behavior, which evidences, e.g., in occurring isolated color spots on the map. Such dramatic change in electron distribution can be attributed to emergence of a specific phonon-assisted trajectories (complex Bloch oscillation) which is shown as a solid curve in Fig. 5(c), recounting a wave packet moving slowly in the proximity of $p_x = 0$ and quickly at $p_x = \hbar\pi/d$. This type of trajectories appear for $U > U_{\text{cr}_1}$ in addition to another low-amplitude regular p_x trajectory [dashed curve, Fig. 5(c)] which existed also for $U < U_{\text{cr}_1}$. The latter one (dashed curve) indicates a wave packet moving quickly around the center of the Brillouin zone, corresponding to the confined electron motion within the propagating moving potential. These two types of trajectories differ by their initial values x_i . The motion of the electrons starting from certain initial conditions such as the solid trajectory in Fig. 5(c) experiences Doppler instability accompanied either by phonon absorption (red wavy arrow) or emission (green wavy arrow) which give rise to oscillations of electron bunches with larger amplitude. Figure 5(d) illustrates the balance between kinetic \mathcal{E} and potential energy V for phonon absorption or emission processes. In an absorption process, a wave packet with a small crystal momentum $p_x \sim 0$, gains a considerable portion of energy while moving [red dashed arrow, Fig. 5(d)] from the bottom to the top of the miniband at the expense of potential energy [red curve, Fig. 5(d)]. In contrast, during the emission process, a wave packet with a large p_x (near $p_x = \pi \hbar/d$) loses a considerable part of its energy [green dashed arrow, Fig. 5(d)]

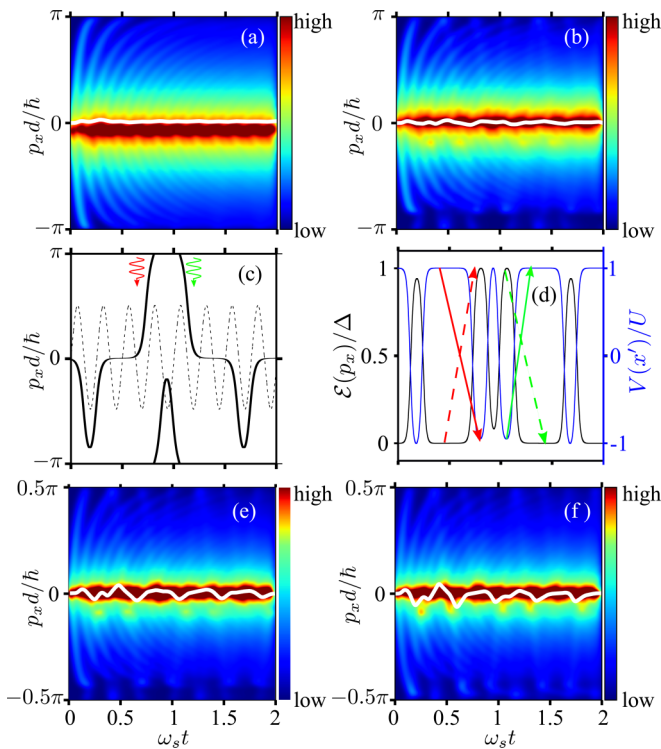


FIG. 5. The temporal dynamics of the reduced electron distribution function $\tilde{f}(p_x, t)$ before the first bifurcation (a) $2U/\Delta = 0.95$ and just after (b) $2U/\Delta = 0.98$ with the red region in the colormap indicating the formation of the electron bunch. (c) p_x -space trajectories for $2U/\Delta = 0.98$ ($U_{\text{cr1}} < U < U_0$) and different initial conditions: $x_0 = 0$, trapped trajectory (dashed line) in the acoustic wave potential and $x_0 \approx -\pi/(2k_S)$, trajectory (solid line) which experiences anomalous Doppler instabilities. The wavy arrows indicate the absorption (red) and the emission (green) of phonons. (d) The temporal oscillations of miniband energy (black curve) and potential energy (blue curve) for $2U/\Delta = 0.98$ ($U_{\text{cr1}} < U < U_0$) and the initial condition $x_0 \approx -\pi/(2k_S)$. (e), (f) The temporal dynamics of the reduced electron distribution function $\tilde{f}(p_x, t)$ indicating the electron bunch (red) for different wave amplitudes: (e) $2U/\Delta = 1$ ($U = U_0$) and (f) $2U/\Delta = 1.04$ ($U_{\text{cr1}} < U < U_{\text{cr2}}$). The white lines designate the mean of electron quasimomentum distribution (mean angle $p_\phi = p_a d/\hbar$) as a function of time. The calculations have been performed using the parameters of the SL structure with $v_e/v_s = 22$.

while a making a transition from the top to the bottom of the potential [green arrow, Fig. 5(d)]. Each radiation act is preceded (followed) by extended presence of electron around the center of the Brillouin zone. Considering now an electron ensemble, the electron wave packets are concentrated around a single trajectory [white curve in Fig. 5(b)] with mean value p_a that oscillates further close to the center of BZ in comparison to the trajectory in Fig. 5(a), causing the electron bunches to slow down; see the sudden drop of v_m in the inset of Fig. 4. At $U = U_0$, the electrons eventually become localized. In this case, the averaged momentum p_a [white curve in Fig. 5(e)] oscillates almost periodically around $p_x = 0$ resulting in a zero v_m . For $U > U_0$ the electronic bunches counter-propagate with respect to the propagating sound wave. Such inversion of motion becomes apparent in Fig. 5(f), where the electron bunch is shifted below $p_x = 0$. The inversion of electrons drift

can be explained by an increase of electron trajectories which are subjected to anomalous Doppler shifts. The backward drift of electrons becomes maximal at U_{cr2} , coinciding with the first manifestation of normal Doppler effect as discussed in Sec. II.

To gain a deeper insight in the emission processes and their implications in electron bunching, we examine in detail the dynamics of averaged parameters in the vicinity of the first bifurcation at $U \approx U_{\text{cr1}}$. Namely, we analyze the characteristics, which beside the averaged momentum p_a (Fig. 5) include the coherence of electron distribution $A = |m_1|$, the averaged electron energy, $E_a = \Delta/2 \langle 1 - \cos\{p_x(t)d/\hbar\} \rangle_{x_i}$, and the averaged potential energy $V_a = -U \langle \sin(k_{sx} - \omega_s t) \rangle_{x_i}$. Note that the electron distribution converges to a Dirac distribution centered on a single trajectory at mean value p_a for $A = 0$, whereas for the opposite limit $A = 1$, there is no well defined mean of the electron momentum. Figure 6(a) shows the dynamics of p_a in time as U growth. For $U < U_{\text{cr1}} = 9.55$ meV ($2U/\Delta = 0.955$), p_a demonstrates a low-amplitude erratic fluctuations (blue curve), which are substituted by more regular close to quasiperiodic oscillations once U exceeds U_{cr1} (red curve). Further growth of U leads to increase of the amplitude of the oscillations that remains quite regular (black curve). Such regularization of the electron bunch dynamics and appearance of pronounced large-amplitude oscillations of p_a is associated with the Doppler instability evoked by the absorption or the emission of phonons, which, as it has been shown above, take place for $U > U_{\text{cr1}}$. Repeating inelastic absorption or emission events perturb also the coherence parameter A which demonstrates larger oscillations for larger U , indicating that electron bunches are created and then deformed almost periodically [compare blue, red, and black curves in Fig. 6(b)]. This further explains the abrupt change in electron distribution and the formation of distinct color spots with time variation as was demonstrated in Figs. 5(e) and 5(f). The effect of the Doppler instability related to phonon exchange can be clearly seen in the time realizations of the kinetic E_a and potential component V_a of the electrons energy, which are presented in Figs. 6(c) and 6(d), respectively. For $U < U_{\text{cr1}}$, the energy the exchange between E_a and V_a is very small [see blue curves in (c) and (d)]. However, if U even slightly exceeds U_{cr1} , the interplay between E_a and V_a dramatically intensify, and become larger for larger U [see red and black curves in (c) and (d)]. The vertical dashed lines in (c) and (d) illustrates the energy transformation. Namely, it indicates a moment when the electron bunch having a large potential energy V_a start to lose it due to phonon exchange events with simultaneous increasing the kinetic component E_a . We note that the concept of a wavelike bunching of the electrons [53–55] in momentum space has already been used to explain the amplification of a THz field which might arise due to the interaction of the bunches with the THz field itself. Extended analysis of the effects of the scattering processes on miniband transport and sound absorption will be presented in the following section.

IV. NONLINEAR ELECTRIC TRANSPORT AND THE SOUND ATTENUATION EFFECTS

Up to now, we have considered the quasiballistic regime, i.e., $\alpha = k_s l \gg 1$, to study the role of the acoustoelectric

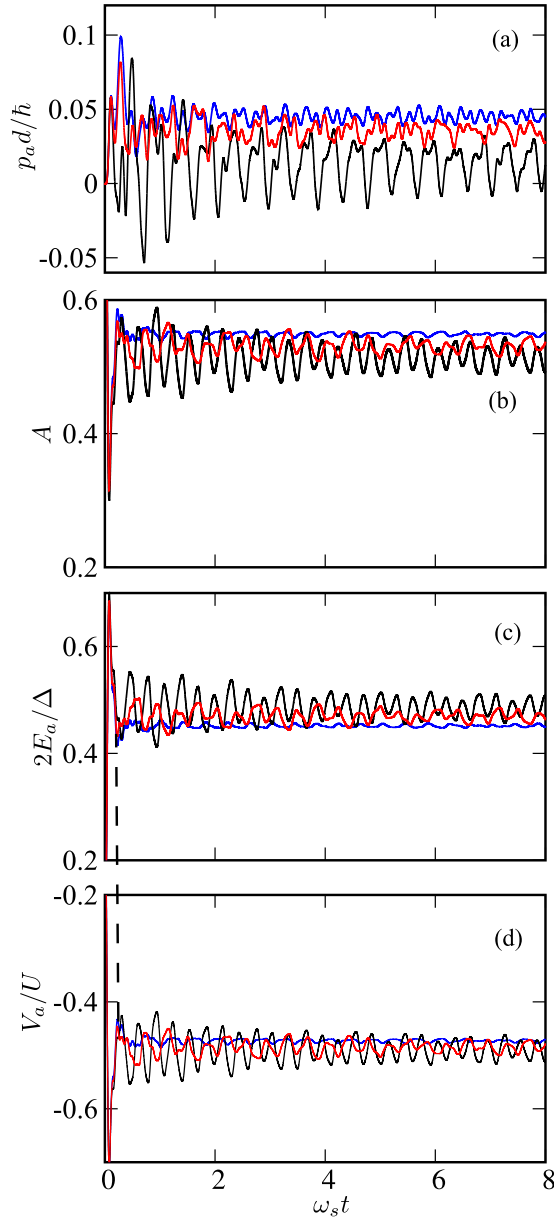


FIG. 6. The numerically obtained oscillations of (a) the averaged momentum p_a , (b) the coherence, A , of the electron distribution, (c) the averaged electron energy E_a , and (d) the averaged potential energy V_a for $2U/\Delta = 0.95$ ($U < U_{cr1}$, blue curves), $2U/\Delta = 0.96, 0.98$ ($U_{cr1} < U < \Delta/2$, black and red curves). The calculations have been performed using the parameters of the SL structure with $v_e/v_s = 22$. Dashed vertical line is discussed in text.

effects in the quasiclassical description of the electron transport. However, the effects of coherent phonon dynamics on the miniband electrons and the related superluminal phenomena might appear over a wide range of the parameter α , as it was previously shown for electron phonon interactions in metals [40,56]. A more general approach is to take into account the scattering effects, when the mean free path, $l = v_0\tau$, is comparable with to the sound wavelength λ . In this case, to describe the directed electron transport in a superlattice we use the Boltzmann transport Eq. (17) with $\text{St}[f] = (f_0 - f)/\tau$, where τ is the relaxation time and $f_0(x, p_x)$ is the Fermi

distribution in the nondegenerate limit. Solution of BTE yields the drift velocity of electrons

$$v_d = \int_0^{T_s} \frac{dt}{T_s} \int_{-\infty}^t e^{-\frac{(t-t_i)}{\tau}} v_x(t, t_i) \frac{dt_i}{\tau}. \quad (20)$$

Here t_i is the time of last collision at position x_i , $v_x(t, t_i)$ is a trajectory in time governed by Eqs. (4) and $T_s = 2\pi/\omega_s$ is the period of the acoustic plane wave. To simplify analysis, we utilized a constant scattering time approximation. With this, the relaxation rate τ in Eq. (20) can facilitate both elastic scattering processes and additional inelastic scattering processes due to long wave phonons [57] as an inverse summation of all corresponding scattering times [58]. Usually, the relaxation time depends on electron energy [59]. However, superlattices typically have narrow band width (miniband) and therefore in many cases the energy dependence of τ can be considered as negligible [60]. Despite such simplicity, the constant scattering time approximation was shown to demonstrate a good agreement both with the full-scale Monte Carlo simulations of various transport phenomena in SLs [54,55,61] as well as with experimental results on charge transport in SLs [57,62] including high-frequency current oscillations induced by coherent phonons [15]. Eq. (20) can be obtained using the time-dependent path-integral approach [63–65] which allows to investigate generic features of electron transport and unravel the acoustoelectric effects that might arise in the system. To analyze the deformation propagation in a SL we additionally take into account the back action of electrons on the phonon wave by considering the sound attenuation effects. In general, the electron contribution to the attenuation of the ultrasound in materials arises because energy is transferred between the wave and electrons. Therefore the absorption coefficient of the sound is given by [36,66,67]

$$\Gamma = \int \langle \dot{H}(p_x, t) f(p_x, x, t) \rangle_{T_s} dp_x. \quad (21)$$

Here $\dot{H} = dH/dt$, whereas the angle brackets designate averaging over time, namely the period of the sound wave $T_s = 2\pi/\omega_s$. By solving Eq. (21), we find (see Appendix C) the absorption coefficient of the sound in the SL miniband, which is presented for our convenience in a normalized form

$$A_s = \left\langle \left(\tilde{v}(t) - \frac{v_s}{2v_0} \right) \cos(k_s x - \omega_s t) \right\rangle_{T_s}, \quad (22)$$

where the absorption coefficient Γ is related to A_s as $\Gamma = (2k_s U) A_s$ and $\tilde{v}(t) = \langle v_x(t) \rangle / v_0$ is the electron velocity averaged over the distribution function, f , satisfying the BTE [Eq. (17)]. The dependence of the drift velocity v_d on U for an acoustic wave with $\omega_s = 0.1\tau^{-1}$ ($\alpha \sim 1.3$) and a superlattice with a miniband width of 7 meV ($v_0/v_s = 13$) is presented in the left-hand panel of Fig. 7(a). One can recognize two characteristic values of U . First, the drift velocity is drastically suppressed beyond $U = U_{cr1}$ and subsequently the $v_d(U)$ characteristic exhibits an observable change in slope at $U = U_{cr2}$. The black solid curve in Fig. 7(a) reminds the classical Esaki-Tsu $v_d(E_{dc})$ [37], which describes the response of miniband electrons to an electric field E_{dc} , applied along the growth direction of the superlattice. However, in our case the specific changes in v_d with variation of U

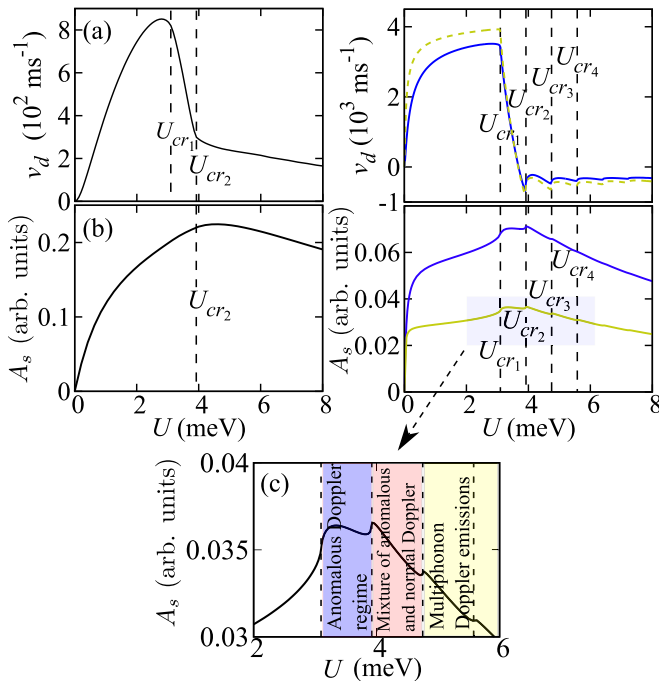


FIG. 7. (a) The dependence of the drift velocity v_d as a function of the acoustic wave amplitude U . The left panel demonstrates $v_d(U)$ for the wave frequency $\omega_s = 0.1\tau^{-1}$ whereas the right panel for $\omega_s = 0.5\tau^{-1}$ (dashed yellow curve) and $\omega_s = \tau^{-1}$ (blue curve). (b) The dependence of the absorption coefficient of the sound wave $A_s = \Gamma/(2k_s U)$ upon U calculated for different frequencies: $\omega_s = 0.1\tau^{-1}$ (left), $\omega_s = 0.5\tau^{-1}$ (right, blue curve) and $\omega_s = \tau^{-1}$ (right, yellow curve). (c) Zoom in of (b)—right panel, showing the different regimes of phonon emissions. The vertical lines designate the critical values of U . The calculations have been performed using the parameters of the SL structure with $v_0/v_s = 13$; See Tables II and III.

are directly associated with changes in the electron bunches dynamics, revealing the appearance of the superluminal effects as discussed in Sec. III. Hence, the critical amplitudes U_{cr_1} and U_{cr_2} designated by the vertical lines in Fig. 7(a) correspond to the thresholds for triggering the superluminal anomalous and superluminal backward Doppler effects that are associated with emission and absorption of phonons in the presence of scattering. Figure 7(b) demonstrates the behavior of A_s with change of U . The increase of U first enhances the absorption of the acoustic wave, since its interaction with the electrons becomes stronger. However, once U reaches U_{cr_2} , the absorption starts to drop gradually. Such reduction of A_s relates to the rise of normal Doppler effects resulting from the recoil momentum given to the radiating system by the emitted phonons. The changes in $v_d(U)$ and $A_s(U)$ indicating transitions between different superluminal regimes which become more evident for acoustic driving with higher frequency ω_s . In the right panel of Fig. 7(a), the dependencies $v_d(U)$ are shown for $\omega_s = 0.5\tau^{-1}$ ($\alpha \sim 6.6$) by dashed yellow curve and $\omega_s = \tau^{-1}$ ($\alpha \sim 13.2$) by solid blue curve. Both dependencies have pronounced features at the same values of U . However, in contrast to the low-frequency case presented in the left panel Fig. 7(a) the high-frequency dependencies indicate more features also related to U_{cr_n} (9) for $n > 2$. Importantly, these high-frequency (short-wavelength) acoustic excitations

can induce the reverse of the electron drift ($v_d < 0$) due to mechanisms discussed in Sec. II. The features in the graph of $v_d(U)$ are also reflected in the dependence $A_s(U)$ shown in the right-hand panel of Fig. 7(b). For example, a kink in $A_s(U)$ at U_{cr_1} in Fig. 7(b) coincides with the maximum of $v_d(U)$ in Fig. 7(a). A local minimum of A_s at $U = U_{cr_2}$ corresponds to the reverse of drift velocity v_d . Other abrupt changes in v_d are observed when $A_s(U)$ attains the minima [see Fig. 7(b)] at U_{cr_n} for $n = 3$ and 4. The appearance of these kinks, i.e., local minima in $v_d(U)$, $A_s(U)$ can be attributed to the transition between different superluminal regimes of phonon emission. Figure 7(c) illustrates these regimes considering a zoomed part of yellow curve $A_s(U)$ from the right panel of the Fig. 7(b). They include (i) an anomalous Doppler regime ($U_{cr_1} < U < U_{cr_2}$) indicated by the blue shaded area in Fig. 7(c) where a significant portion of electron trajectories experiences anomalous Doppler instabilities which start to move backwards leading to the suppression of drift velocity and considerable reduction in the sound absorption coefficient. (ii) Coexistence of anomalous and normal Doppler effects ($U_{cr_2} < U < U_{cr_3}$). In this regime, an increase of U enables more charged particles to experience normal Doppler instabilities resulting in emission of phonons at the expense of electron trajectories which are subjected only to anomalous Doppler instabilities. Hereafter, the overall drift of electron bunches remains negative whereas the absorption of the sound wave is further reduced. (iii) Multiphonon Doppler processes ($U > U_{cr_3}$) in which the electrons are inelastically scattered by the acoustic wave allowing their trajectories to enter successively higher Brillouin zones. These more complicated trajectories are responsible for the further suppression of the absorption coefficient.

V. ABSOLUTE NEGATIVE MOBILITY

In previous Sec. IV, we studied the superluminal mechanisms governing the directed electron transport in a strongly coupled SL subjected to a sole acoustic plane wave. Next, we consider the absolute negative mobility (ANM) and the superluminal Doppler effects which go hand in hand in case a constant electric field E_{dc} is additionally applied along the SL. The ANM has been already reported [33] in DC-biased SLs under high frequency irradiation $\propto E_{\Omega} \cos(\Omega t)$, shown as inversion of electron current in the vicinity of $E_{dc} = 0$. In our model, the acoustic drive oscillates both in time and space and thus the semiclassical equations of motion for the miniband electrons are

$$v = v_0 \sin\left(\frac{p_x d}{\hbar}\right), \quad (23a)$$

$$\frac{dp_x}{dt} = eE_{dc} + k_s U \cos[(k_s(x + x_i) - \omega_s t)], \quad (23b)$$

where $e > 0$ is the elementary charge. Figure 8 shows the dependencies of drift velocity v_d as a function of the electric field E_{dc} numerically calculated for different amplitudes of U . For our calculations we chose the parameters close to ones from recent experiments [16], $\Delta = 20$ meV and $\omega_s = 0.1\tau^{-1}$ ($\alpha \sim 3.5$). For a weak acoustic excitation (black solid and black dashed curves), $v_d(E_{dc})$ is almost identical to the

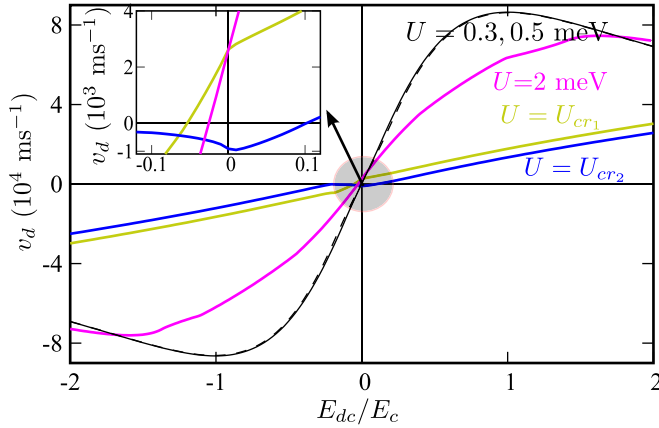


FIG. 8. Drift velocity-electric field characteristics with variation of the wave amplitude $U = 0.3, 0.5,$ and 2 meV and at the critical values of the instabilities $U_{cr1} = 9.55$ meV and $U_{cr2} = 10.46$ meV. $E_c = 2.3$ kV/cm is the critical field for the onset of NDV in the Esaki-Tsu characteristic. The solid and dashed black lines indicate the $v_d(E_{dc})$ characteristics for small wave amplitude at $U = 0.3$ and 0.5 meV, respectively. The frequency of the acoustic wave is fixed at $\omega_s = 0.1 \tau^{-1}$ ($\alpha \sim 3.5$). The calculations have been performed using the parameters of the SSL structure with $v_0/v_s = 35$; see Table II.

Esaki-Tsu dependence [37]. Therefore the supersonic condition ($v_d > v_s$) for the Cherenkov emission can exist for $U \ll U_{cr1}$, however it does not necessary produce ANM or result in the suppression of the drift velocity. This was confirmed in the recent experiments [16], which have shown that the current-voltage characteristics are almost identical with or without illumination of the SL sample by the femtosecond pulse train resulting the coherent acoustic wave generation due to stimulated Cherenkov phonon emission. However, as the value of U increases the dependence become less and less steeper, compare pink curve for $U = 2$ meV, yellow curve $U = U_{cr1} = 9.55$ meV and blue curve for $U = U_{cr2} = 10.46$ meV. The mechanisms of such a suppression [12,15] are similar to the mechanisms governing the electron transport in a DC-biased SL under electromagnetic irradiation [33]. They relate to the fact that the electron tunneling probability is affected by the energy $\hbar\omega$ of the excitation quantum of frequency ω , which could be either photon ($\hbar\Omega$) or phonon ($\hbar\omega_s$) interacting with the electron. Here, the drift velocity can be expressed in terms of the phonon-assisted replicas of the Esaki-Tsu drift velocity [12,68],

$$v_d \sim \sum_{n=-\infty}^{\infty} J_n^2(\beta) v_{d0}(E_{dc}d + n\hbar\omega_s/e), \quad (24)$$

where J_n is the first-kind Bessel function of order n , $v_{d0}(E_{dc})$ is the dependence of the electron drift velocity on the DC bias E_{dc} for SL in the absence of photon/phonon excitations, $\beta = edE_s/(\hbar\omega_s)$ and $E_s = k_s U/e$ is voltage equivalent of the magnitude of the acoustic wave driving the SL. For a range of β the term with J_0 produces a dominant effect, so implying suppression of the v_d with growth of U . The validity of Eq. (24) for the phonon-assisted transport is limited either to small amplitude β (black curve, Fig. 8) or to the quasistatic limit $a = k_s l \ll 1$ [69]. Thus we resort instead to the fully

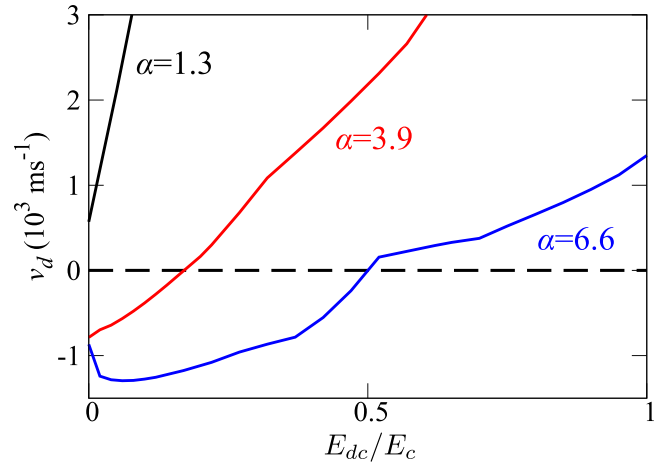


FIG. 9. Dependence of the drift velocity v_{dc} on the dc bias E_{dc} for the amplitude of the acoustic wave $U = U_{cr2} = 3.92$ meV and for different sound frequencies: positive slope for $\omega_s \tau = 0.1$ ($a = 1.3$, black curve), ANM for $\omega_s \tau = 0.3$ ($a = 3.9$, red curve) and $\omega_s \tau = 0.5$ ($a = 6.6$, blue curve). $E_c = 2.1$ kV/cm is the critical field for the onset of NDV in the Esaki-Tsu characteristic. The calculations have been performed using the parameters of the SSL structure with $v_0/v_s = 13$; see Table II.

numerical integration of the model Eq. (23) and calculation of drift velocity via BTE solution Eq. (20) which indicate that ANM takes also place for a propagating acoustic excitation. In particular, we found that for selected values of the SL parameters, ANM is realized when U exceeds $U_0 = 10$ meV. Since $U_{cr1} < U_0 < U_{cr2}$, it indicates the gradual onset of the ANM due to the absorption and emission of phonons under the conditions of the anomalous Doppler effect. The inset of Fig. 8 illustrates a zoomed part of the main panel of Fig. 8 in vicinity of $E_{dc} = 0$ and it reveals a negative drift of the electrons ($v_d < 0$) for $E_{dc} = 0$ when $U = U_{cr2} = 10.46$ meV (blue curve) and positive v_d when $U = U_{cr1} = 9.55$ meV (yellow curve) or $U = 2$ meV (pink curve). It follows that the condition for near zero mobility of an acoustically driven SL can be given by

$$E_s = \alpha E_c. \quad (25)$$

Here, we have rewritten localization condition Eq. (19) in terms of the amplitude, E_s of the effective acoustoelectric field, whereas $E_c = \hbar/(ed\tau)$ is the critical electric field for the onset of the negative differential velocity (NDV) in Esaki-Tsu characteristic [37]. In contrast, the localization condition [33,68] for the photon-assisted transport is $J_0(\beta) = 0$ with the first root given at $\beta = E_\Omega/(E_c \Omega \tau) \sim 2.4$. Furthermore, the dynamic localization and ANM are not possible for any ac field amplitude when $\Omega \tau < 1$ and therefore the smallest amplitude of an ac field which can induce ANM is $E_\Omega = 2.4 E_c$ at $\Omega = 1/\tau$ [70]. In Sec. IV and Appendix E, we noticed that Doppler effects start to have more prominent implications in directed transport once the sound wavelength becomes comparable with the mean free path of the charge carrier, i.e., $\alpha/(2\pi) \gtrsim 0.5$. This is further confirmed by Fig. 9 showing that the increase of sound frequency ω_s and therefore of α results in the appearance of ANM ($\alpha = 3.9$, red curve) similar to

Fig. 8 in which we have considered a slightly smaller $\alpha = 3.5$. Hereafter, Eq. (25) indicates values that are comparable with the minimum amplitude of ac field which can induce ANM but with considerably lower oscillating frequencies. On the other hand, for α close to zero, i.e. low sound frequencies or SL structures with extremely narrow minibands [71] and therefore smaller v_0 , onset of ANM is not feasible. In this limit, the acoustic wave driving acts practically like a quasistatic ac signal, whereas the electron drift can be described well by Eq. (24).

VI. BROADBAND AMPLIFICATION OF EM WAVES

In this section, we consider amplification of high-frequency electromagnetic waves in acoustically driven SLs [see Fig. 1(b)] and the corresponding role of the Doppler effects, which result in the gain similar to the Bloch gain in electrically biased SLs [34,35]. In this study, we consider the model Eq. (23), in which the Eq. (23b) is substituted by

$$\frac{dp_x}{dt} = eE_\omega \cos(\omega t) + k_s U \cos[(k_s(x + x_i) - \omega_s t)], \quad (26)$$

with the term $E(t) = E_\omega \cos(\omega t)$ designating a weak probe field of the amplitude E_ω and frequency ω . Note that in practice, the frequency ω can be favorably tuned by an external resonant cavity [72]. The absorption of the probe ac field $E(t)$ is determined by the real part of the dynamical conductivity [73]

$$\sigma_r(\omega) = \frac{2\langle j(t) \cos(\omega t) \rangle}{E_\omega}, \quad (27)$$

where $j(t) = eNv_d(t)$ is the time-dependent current generated by the SL driven by the acoustic wave which is calculated using the time-dependent drift velocity

$$v_d(t) = \int_{-\infty}^t e^{-\frac{t-t_i}{\tau}} v_x(t, t_i) \frac{dt_i}{\tau}, \quad (28)$$

similar to the semiclassical approach presented in Sec. IV, whereas the ballistic trajectory $v_x(t, t_i)$ is now governed by Eqs. (4a) and (26). Within this framework, the absorption corresponds to $\sigma_r(\omega) > 0$ and gain to $\sigma_r(\omega) < 0$. The Drude conductivity of the SL is $\sigma_0 = 2j_p/E_c$, where $j_p = eNv_0$ is the peak current density, directly proportionally to electron density N . Here, $\sigma_r(\omega)$ is estimated for a superlattice with a miniband width (20 meV) sufficiently smaller than the optic phonon energy in GaAs [74] and a pump frequency $\omega_s \tau = 0.1$. The magnitude of the acoustic wave's frequency corresponds to $\alpha = 3.5$. The proper choice of α -parameter is important for the appearance of electron bunches with a negative drift and ANM, which indicate strong involvement of Doppler effects, and for controlling interaction between bunches and the probe field, see Appendix E for more details.

Figure 10 illustrates how the absorption profile $\sigma_r(\omega)$ is affected by the variation of U . For small wave amplitude $U = 1.2$ meV, $\sigma_r(\omega)$ (green dash-dotted curve) almost follows the free-carrier absorption (red curve) in the absence of a pump field, demonstrating a power-like decay as probe frequency ω increases, i.e., $\sigma_r \propto (1 + \omega^2 \tau^2)^{-1}$. Comparison

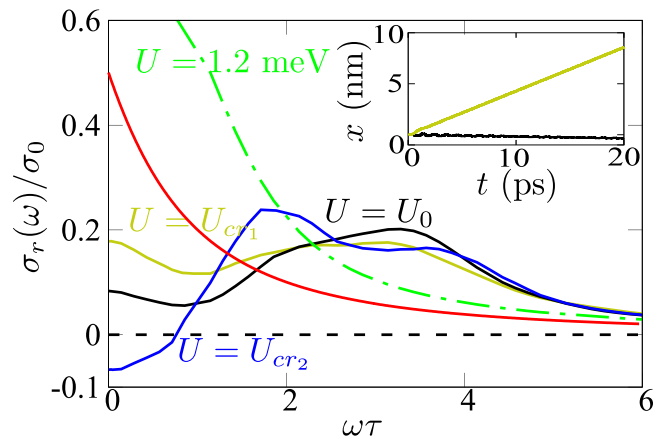


FIG. 10. Absorption and gain profiles, $\sigma_r(\omega)$, at fixed $\omega_s = 0.1\tau^{-1}$ and different values of wave amplitude ($U=1.2$ meV, $U_{cr1} = 9.55$ meV, $U_0 = 10$ meV, and $U_{cr2} = 10.46$ meV). The red curve signifies the free-carrier absorption whereas the horizontal dashed line marks the zero absorption. (Inset) Averaged position of ballistic electron trajectories, $x_a(t)$, calculated for $U = U_{cr1}$ (yellow curve) and U_0 (black curve). The calculations have been performed using the parameters of the SL structure with $v_0/v_s = 35$; see Table II.

of the absorption profiles calculated for $U = U_{cr1}$ (yellow), U_0 (black), and U_{cr2} (blue) shows that as U grows, the low-frequency absorption gradually decreases, and for U close to U_{cr2} a low-frequency gain is realized in the system, see blue curve for $U = U_{cr2}$. This transition originates from the emergence of phonon-assisted Bloch oscillations which are associated with the anomalous Doppler effect. As we showed earlier in Sec. II, at $U \approx U_{cr1}$ the electrons start to demonstrate the Doppler instabilities that obey the first selection rule [see Eq. (13)]. As a result electron bunches are formed, which include the frequency-modulated Bloch oscillations with maximal frequency $\omega_B^{\max} = k_s U d / \hbar$ [24,25]. Appearance of such trajectories decreases absorption for low frequencies ω . Indeed, the absorption profile calculated for $U = U_{cr1}$ (yellow curve) shows significantly lower low-frequency absorption as compared to one for $U = 1.2$ meV (green curve), with the second maximum of absorption in the vicinity of ω_B^{\max} , which for the given parameters corresponds to $\omega\tau \approx 3.3$. Further increase of U can localize electrons drift, see the inset illustrating the averaged ballistic electron trajectories calculated for $U = U_{cr1}$ (yellow) and for U_0 (black). This localization leads to further decrease of absorption for low-frequency range of electromagnetic probe field, compare black and yellow curves in the main panel of Fig. 10. For large enough U , the Doppler effects become more and more prominent, and the drift of electron bunches can eventually be reversed. These mechanisms create a condition for appearance of a low-frequency gain ($\sigma_r(\omega) < 0$) as it is evidenced by the absorption profile calculated for $U = U_{cr2}$ (blue line). The numerical calculations reveal that for the chosen parameters and $U = U_{cr2}$, the gain is possible for the wide range of frequencies up to $\omega/(2\pi) = 480$ GHz. Further analysis showed that $\sigma_r(\omega)$ can obtain a significant THz gain value ($\sigma_r \approx -0.07\sigma_0$) at $U = U_{cr2}$, comparable with the maximum gain of a merely dc-biased superlattice (i.e., canonical Bloch

oscillator): $\min\{\sigma_r(\omega)/\sigma_0\} = -1/8$ at $E_{dc}/Ec = \sqrt{3}$ [73] and larger than expected from SLs driven by monochromatic and polychromatic fields with oscillating frequencies at the sub-THz range [75]. Normally, we relate the magnitude of the gain α_g in units cm^{-1} to dynamical conductivity as $a_g = a_0(\sigma_r/\sigma_0)$ with $a_0 = 1/(c\sqrt{\epsilon\epsilon_0}) \times 2j_p/E_c$ [75,76]. This means that one can acquire the value $a_g = 37 \text{ cm}^{-1}$ for $a_0 \approx 527 \text{ cm}^{-1}$ given a temperature of few millikelvins, moderate doping $N = 10^{16} \text{ cm}^{-3}$ and relative permittivity $\epsilon = 13$ corresponding to GaAs.

VII. CONCLUSION

In this work, we theoretically studied the physical mechanisms of acoustoelectric effects associated with miniband charge transport in semiconductor superlattice. Our analysis reveals that superluminal effects, previously described within the framework of Ginzburg-Frank-Tamm theory for electro-magnetic radiation [21,22,29], play an important role in acoustically (strain) driven electron transport in minibands. In particular, our results suggest the realization of superluminal anomalous Doppler and backward normal Doppler effects which are related to the development of dynamical instabilities for certain magnitudes of acoustic stimuli propagating through a superlattice structure. A kinetic model, based on a semiclassical nonperturbative approach demonstrates that these effects induced by coherent phonons manifest themselves in excitation of complex Bloch oscillations and formation of electron bunches which can counter-propagate or be localized with respect to the propagating deformation pulse. Such character of electron transport is reflected in characteristic kinks in the dependence of electron drift velocity upon the acoustic wave amplitude, and can even lead to the absolute negative mobility. Remarkably, our calculations indicate that the anomalous Doppler effect for supersonic miniband electrons (effectively superluminal) enables realization of a highly tunable gain similar to the Bloch gain occurring in the voltage driven superlattices [34]. These findings open additional avenues for development of efficient acoustoelectronic devices for microwave and THz ranges by providing alternative means for manipulations of electromagnetic waves in various superlattice electronic devices (SLEDs) [62,77] including harmonic multipliers [78,79] and heterostructure millimeter-wave detectors [80]. Since semiconductor superlattices serve as building blocks for quantum cascade lasers (QCLs), our theory provides with helpful guidelines for the investigation of unusual acoustoelectric phenomena in QCLs [81], which can be employed for tuning QCL's broadband THz emission [82]. In this context, it would be useful to investigate the microscopic effects of different scattering mechanisms, such as scattering of electrons by interface roughness and electron-impurity interaction [83], on the reported phenomena. For this aim, one could use Monte Carlo simulation or/and utilize the approaches similar to the [84,85].

In a wider context, similar phenomena can be expected in other miniband systems subjected to slowly propagating excitations such as ultracold atoms in optical lattices [86] or in the physical systems with similar Hamiltonians, e.g., the driven Harper models [87].

ACKNOWLEDGMENTS

A.A. acknowledges financial support by the Czech Science Foundation (GAČR) through Grant No. 19-03765. Research of K.N.A. was partially supported by Marius Jakulis Janson Foundation. F.V.K. acknowledges financial support from FSU-2021-030/8474000371.

APPENDIX A: NONLINEAR DYNAMICS IN THE REST FRAME OF THE ACOUSTIC WAVE

The system dynamics describing the motion of an electron under the influence of a propagating wave potential is described by Eq. (4). To conceptualize how the acoustoelectric phenomena discussed in terms of waves and quanta are related to bifurcations mechanisms, we analyze the equations of motion in the moving reference frame $x'(t) = x(t) + x_i - v_s t$. In this frame, the electron is subjected to a time-independent potential $V(x') = -U \sin(k_s x')$ whereas the kinetic energy of an electron is translated into $\mathcal{E}'(p_x) = \mathcal{E}(p_x) - v_s p_x$. After this transformation, the Hamiltonian becomes

$$H' = \mathcal{E}'(p_x) + V(x') \quad (\text{A1})$$

and therefore the equations of motion can be cast as

$$\dot{x}' = v_0 \sin\left(\frac{p_x d}{\hbar}\right) - v_s, \quad (\text{A2a})$$

$$\dot{p}_x = k_s U \cos(k_s x'), \quad (\text{A2b})$$

which in contrast to Eqs. (4) have no explicit dependence on time in their right-hand sides. It follows that the equilibria of the dynamical system Eq. (A2) should meet the following conditions:

$$v_0 \sin\left(\frac{p_x d}{\hbar}\right) = v_s, \quad (\text{A3a})$$

$$\cos(k_s x') = 0. \quad (\text{A3b})$$

This dictates the locations of the fixed points

$$x' = \frac{\pi}{2k_s} + \frac{m\pi}{k_s}, \quad (\text{A4a})$$

$$p_x = (-1)^l \frac{\hbar}{d} \sin^{-1}\left(\frac{v_s}{v_0}\right) + l \frac{\hbar\pi}{d}, \quad (\text{A4b})$$

where m and l are arbitrary integer numbers. From a viewpoint of a wider miniband ($v_0 > v_s$) and therefore higher conduction current, a simple stability analysis reveals that all these fixed points are always either hyperbolic or elliptic points. After dividing Eqs. (A2b) by (A2a) and performing integration, we obtain the phase trajectory equation

$$x = \frac{(-1)^j}{k_s} \sin^{-1} \left\{ \sin k_s x_i - \frac{\hbar v_s}{U d} \left[\frac{v_0}{v_s} \left(\cos \frac{p_x d}{\hbar} - \cos \frac{p_i d}{\hbar} \right) + \frac{p_x d}{\hbar} - \frac{p_0 d}{\hbar} \right] \right\} + j \frac{\pi}{k_s}, \quad (\text{A5})$$

where j is an integer number, and (x_i, p_i) is an initial condition.

Cherenkov effects near fixed points. We now answer the question whether our moving particle with velocity $v(p_x)$ larger than v_s , is able to induce phenomena analogous to

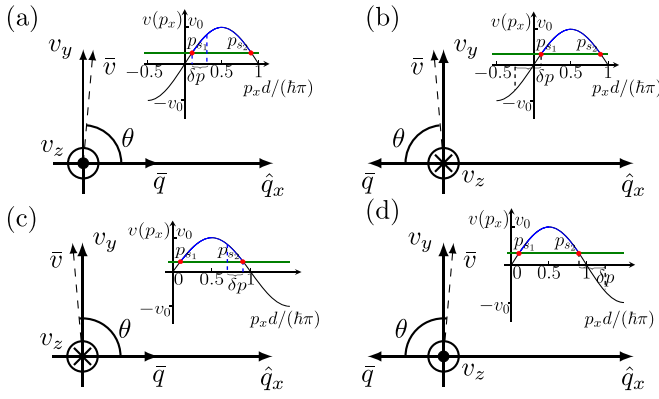


FIG. 11. Schematic representation in the \bar{q} - \bar{v} space of the forward and the backward Cherenkov effects when a charged particle is moving with a supersonic velocity $v(p_x)$ at the center and the borders of the superlattice Brillouin zone. (a) Forward Cherenkov absorption in the proximity of p_{s_1} . (b) Forward Cherenkov emission in the proximity of p_{s_1} . (c) Backward Cherenkov absorption in the proximity of p_{s_2} . (d) Backward Cherenkov emission in the proximity of p_{s_2} . The angle of θ is the opening angle of the Vavilov-Cherenkov cone indicating an almost perpendicular orientation of the velocity vector \bar{v} with respect to abscissa-located phonon wave vector \bar{q} for $U \ll U_{\text{cri}}$. The insets demonstrate the projection of Cherenkov effects in the active zone described by Fig. 2.

Cherenkov-like conical flow and how the stationary points can help to probe these effects. Strictly speaking, to answer this question one should then take into consideration a realistic three-dimensional description by including a quadratic isotropic dispersion law in the Hamiltonian [Eq. (3)] for the in-plane kinetic momentum components $p_{\parallel} = (p_y, p_z)$. However, the forward and reversed Cherenkov radiation, in the proximity of the stationary points, is consistent with the assumption of the 1D emission in Eq. (5) being finitely small. This implication is easily understood by considering an electron with $v_s/v(\bar{p}) \ll 1$ with \bar{p} the total electron momentum. In that case, the Cherenkov mechanism¹ acts mainly in a direction \hat{q}_x almost perpendicular to electron velocity \bar{v} with its x component being the scalar projection \bar{v} onto $\bar{q} = q\hat{q}_x$:

$$\text{comp}_{\bar{q}}\bar{v} = |\bar{v}| \cos \theta = \frac{q}{|q|} v_0 \sin(p_x), \quad (\text{A6})$$

where θ is the angle between the electron velocity and wave vector \bar{q} of the emitted phonon in the proximity of the stationary points. Hereafter we consider in detail the nature of Cherenkov effects around the center of the first Brillouin zone: (i) when $p_f > p_i = -p_{s_1}$, so that $q > 0$. This results in an absorption of phonon and a positive electron velocity that surpasses sound velocity, which is forward Cherenkov radiation [Fig. 11(a)]. (ii) When $p_f < p_i = p_{s_1}$, so that $q < 0$. This results in an emission of phonon and a negative electron velocity that its norm surpasses sound velocity, which is again forward Cherenkov radiation. Consider now what happens at the border of the first Brillouin

¹This is nothing more than the kinetic description of Cherenkov interactions of sound wave with electrons in metals stemming from Landau absorption mechanism [96].

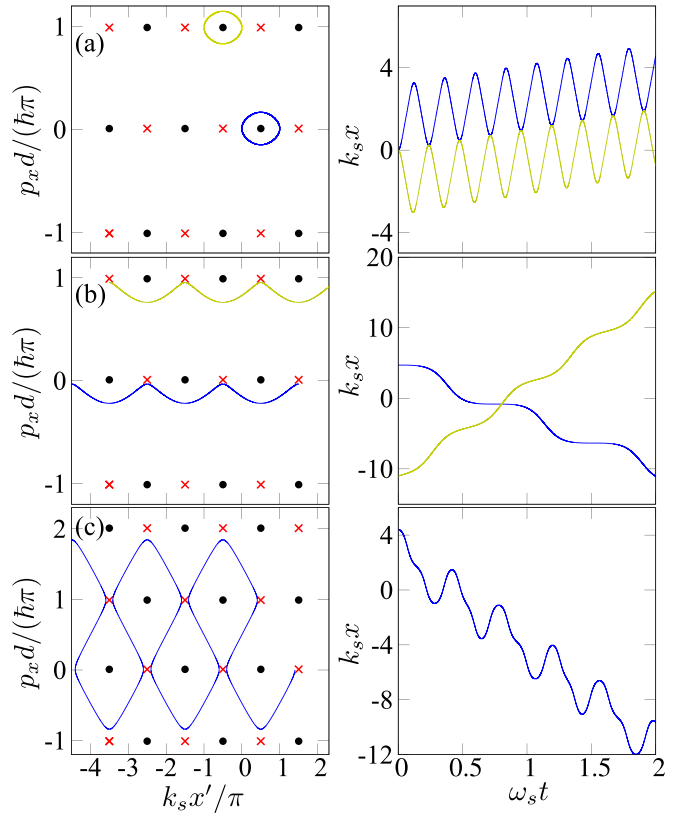


FIG. 12. [(a) and (b)] Phase space trajectories (left) and the related electron trajectories (right) in real space that can determine the nature of Cherenkov effects in the vicinity of the center and the border Brillouin zone for $U = 1.2$ meV. The yellow trajectories correspond to the backward Cherenkov whereas the blue ones to the forward Cherenkov. (c) The complex meandering trajectory and the corresponding trajectory in real space representing the phonon-assisted Bloch oscillation which arises for $U = 10$ meV $> U_{\text{cri}}$. The positions of the elliptic points are depicted by black solid circles and the hyperbolic points by red crosses. The calculations have been performed using the parameters of the SL structure with $v_0/v_s = 35$; see Table II.

zone: (iii) when $p_f < p_i = p_{s_2}$, so that $q < 0$. This results in an emission of phonon and a positive electron velocity with $v > v_s$, which is backward Cherenkov. Finally, (iv) when $p_f > p_i = p_{s_2}$ which may lie outside the first BZ (Umklapp process), so that $q > 0$ and in this sense is an absorption of phonon [Fig. 11(d)]. To find the physically equivalent point inside the first BZ, we have to subtract the module of the reciprocal superlattice vector $|G_0| = 2\pi/d$ from p_f . Thus $p'_f = p_f - |G_0|$ will be found in the proximity of p_{s_3} with $v < 0$ which results in a backward Cherenkov effect. Practically, we have forward and backward Cherenkov-like conical flow in the center and at the edges of BZ respectively. Similar description one can attain from the elliptic points at the center and edges of the BZ, i.e., normal versus backward Cherenkov. In essence, the counter-wise rotation of the phase-space trajectories around the elliptic points [left-handed panel of Fig. 12(a)] with $p_{e_1} = (\hbar/d) \sin^{-1}(v_s/v_0)$ and $p_{e_2} = \pi d/\hbar - (\hbar/d) \sin^{-1}(v_s/v_0)$ designate the nature of the Cherenkov instabilities. Therefore, for absorption of an

infinitely small quasiparticle (q) the clockwise trajectory (blue curve) in the proximity of p_{e_1} is related to an electron trajectory in the real space that moves in the positive direction of x , $v(p_{e_1} + q) > 0$ (forward Cherenkov effect). On the contrary, the electron trajectory which moves momentarily in the negative direction, $v(p_{e_1} + q) < 0$ (backward Cherenkov effect), corresponds to the counterclockwise trajectory (yellow curve). Those two trajectories are directly associated with the motion of electrons confined by the propagation potential and they coexist for small U with unbounded trajectories [left-handed panel of Fig. 12(b)] in the moving reference frame. The latter phase-space trajectories are related to unconfined motion [right-handed panel of Fig. 12(b)] of electrons in real space and their different direction has origin again in the nature of different Cherenkov effects.

Global instabilities (bifurcations). The aforementioned trajectories and the associated Cherenkov effects can well exist both for small and large wave amplitudes. Considering though substantially larger values of U triggers a series of global instabilities which are attributed to instances where the manifold of one hyperbolic point touches another hyperbolic point. It has been shown that the conservation of energy, $H' = \text{const}$ [see Eq. (A1)], can be used to determine the bifurcation points analytically [25]

$$U_{cr} = \frac{\frac{\Delta}{2} [\cos(p_{s_i} d / \hbar) - \cos(p_{s_j} d / \hbar)] + v_s p_{s_i} - v_s p_{s_j}}{\sin(k_s x_{s_j}) - \sin(k_s x_{s_i})}, \quad (\text{A7})$$

where (x_{s_i}, p_{s_i}) and (x_{s_j}, p_{s_j}) are a set of coordinates of hyperbolic points which are involved in a specific bifurcation. Using these coordinates one can attain the explicit formulations for critical values of the wave amplitude, i.e.,

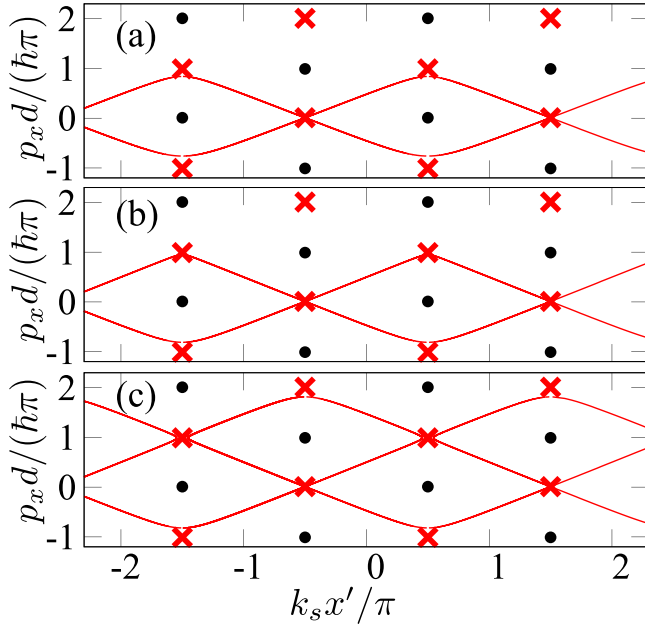


FIG. 13. Separatrix structure in the proximity of the first bifurcation point U_{cr1} for (a) $U = 9$, (b) 9.52, and (c) 9.6 meV. The positions of the elliptic points are depicted by black solid circles and the hyperbolic points by red crosses. The calculations have been performed using the parameters of the SL structure with $v_0/v_s = 35$; see Table II.

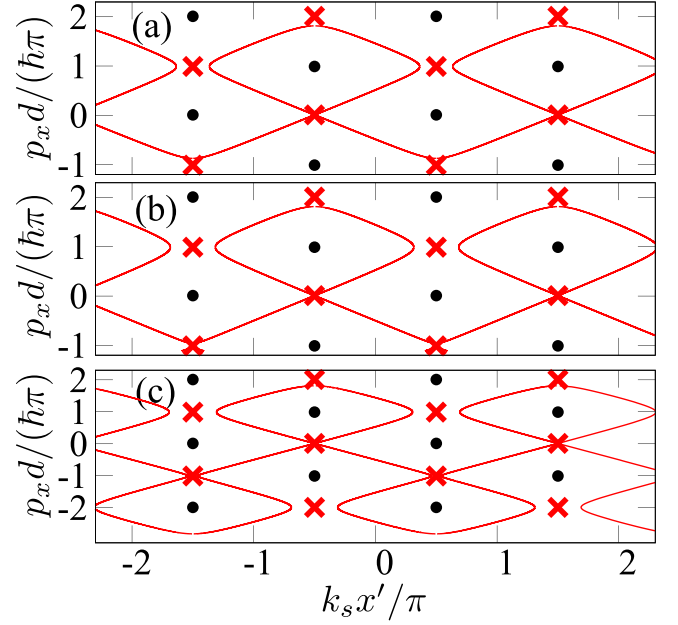


FIG. 14. Separatrix structure in the proximity of the second bifurcation point U_{cr2} for (a) $U = 10$, (b) 10.4, and (c) 10.5 meV. The positions of the elliptic points are depicted by black solid circles and the hyperbolic points by red crosses. The calculations have been performed using the parameters of the SL structure with $v_0/v_s = 35$; see Table II.

Eqs. (9)–(11). The bifurcations cause dramatic transformation of the phase space (see Figs. 13 and 14) and result in the emergence of meandering trajectories such as the one depicted in the left-handed panel of Fig. 12(c) which corresponds to frequency-modulated oscillations in real space shown in the right-handed panel of Fig. 12(c). This trajectory in contrast to the ones depicted in Figs. 12(a) and 12(b) follows from a nonconventional acoustoelectric effect which is an effective counterpart of the superluminal anomalous Doppler effect. The discussion under which conditions this phenomenon arises and how relates to global instabilities are presented in detail in Sec. II.

APPENDIX B: ENSEMBLE-AVERAGED PHYSICAL QUANTITIES

By resorting to ensemble-averaged physical quantities in Sec. III helped us to better understand the role of the Doppler effects in the global transport in the dissipationless limit. In this Appendix, we will discuss in detail the proper definition of these quantities starting from a straightforward approach in which we simply average across the initial positions x_i of electrons, or, equivalently across the initial phases of the acoustic wave

$$v_a(t) = v_0 \left\langle \sin \left\{ \frac{p_x(t)d}{\hbar} \right\} \right\rangle_{x_i}, \quad (\text{B1a})$$

$$E_a(t) = \frac{\Delta}{2} \left\langle 1 - \cos \left\{ \frac{p_x(t)d}{\hbar} \right\} \right\rangle_{x_i}, \quad (\text{B1b})$$

$$V_a(t) = -U \langle \sin(k_s x - \omega_s t) \rangle_{x_i}, \quad (\text{B1c})$$

where $v_a(t) = \langle \dot{x} \rangle_{x_i}$ is the averaged electron velocity, $E_a(t) = \langle \mathcal{E}(p_x) \rangle_{x_i}$ is the averaged electron energy and $V_a(t) = \langle V(x, t) \rangle_{x_i}$ is the averaged potential energy. For example, the value of $\langle v_a(t)x \rangle_{x_i}$ is determined by averaging \dot{x} over an ensemble of electron trajectories with different x_i from the interval $[-\lambda/2, \lambda/2]$. Here, $\lambda = 2\pi/k_s$ designates the space period of the propagating wave. We are ready now to define the dissipationless approach ($\tau \rightarrow \infty$) for the evaluation of (20). Thus one can formally calculate the time-averaged velocity $v_m = \langle v_a(t) \rangle_{\Delta t}$ by using

$$v_m = \frac{1}{\lambda} \int_{-\lambda/2}^{\lambda/2} dx_i \int_0^{\Delta t} v(t, t_i) \frac{dt}{\Delta t} \quad (\text{B2})$$

and the initial conditions

$$x(t_i, t_i) = x_i, \quad p_x(t_i, t_i) = 0. \quad (\text{B3})$$

In this approach, $[v(t, t_i), p_x(t, t_i)]$ plays the role of the Vlasov phase and t_i designates the initial time as described in Refs. [88,89] and references therein.

However, this approach described by Eq. (B1) faces shortcomings when we are seeking to define precisely the averaged momentum p_a , i.e., the center of the mass of the electron distribution (CMED), $f(p_x, x, t)$, in the quasimomentum space. Let us now reduce the dimensionality of $f(p_x, x, t)$ by integrating over all initial phases (from $-\lambda/2$ to $\lambda/2$) of the acoustic wave

$$\tilde{f}(p_x, t) = \langle f(p_x, x, t) \rangle_{x_i}.$$

We may obtain the x_i -averaged quantities [Eqs. (B1a)–(B1c)] that were introduced earlier by averaging against \tilde{f} , $\langle \cdot \rangle_{x_i} = d/(\pi \hbar) \int_{-\pi \hbar/d}^{\pi \hbar/d} \tilde{f}(p_x, t) dp_x$. One can easily understand the implications of such a choice for $\langle p_x \rangle_{x_i}$ by considering the $\tilde{f}(p_x, t)$ centered around a symmetric and narrow peak at $p_x = \pi \hbar/d$. In that case, the expectation value $\langle p_x \rangle_{x_i} = 0$ contradicts the real value of $\pi \hbar/d$. To predict with precision the CMED, we resort to a circular mean angle $p_\phi = p_a d/\hbar$ which is determined by the first trigonometric moment m_1 of the distribution²

$$p_\phi = \arg m_1, \quad m_1 = \langle \exp(ip_x d/\hbar) \rangle_{x_i}, \quad (\text{B4})$$

while the (circular) variance of the distribution is obtained from absolute value, $|m_1| = A$, of the first trigonometric moment

$$\mathcal{V} = 1 - A. \quad (\text{B5})$$

Here the \mathcal{V} takes values between 0 and 1. The value of the lower bound, $\mathcal{V} = 0$, implies a Dirac δ -distribution function centered at mean angle p_ϕ , whereas the value of the upper bound, $\mathcal{V} = 1$, indicates a distribution function which has no defined mean. To analyze though the effects of electron bunching in Sec. III, we shall use A which describes the coherence of the electron distribution, i.e., how concentrated

²This method relies on superlattice balance equations [51] and their connection to rotationally symmetric distributions in directional statistics [52].

is \tilde{f} around its mean. The averaged velocity and averaged energy can be obtained in terms of the variables p_ϕ, A

$$v_a = \frac{A \Delta d}{2 \hbar} \sin(p_\phi), \quad E_a = \frac{A \Delta}{2} [1 - \cos(p_\phi)]. \quad (\text{B6})$$

From Eqs. (B1) and (B6), one finds that

$$A \sin(p_\phi) = \langle \sin(p_x d/\hbar) \rangle_{x_i}, \quad (\text{B7a})$$

$$A(1 - \cos(p_\phi)) = \langle 1 - \cos(p_x d/\hbar) \rangle_{x_i}. \quad (\text{B7b})$$

In fact, our numerical calculations further confirmed that the ensemble average approach [Eq. (B1a)] and the averaging against circular distribution [see Eq. (B6)] of electron velocity are equivalent.

p-space bunching between higher order bifurcations

Figure 15 complements Figs. 5 and 6 by summarizing the properties of wavelike bunching of electrons in momentum space between consecutive higher-order bifurcations. Specifically, we consider three values of U between U_{cr_2} and U_{cr_3} , viz. $2U/\Delta = 1.06, 1.08$, and 1.1 and another three values between U_{cr_3} and U_{cr_4} , namely, $2U/\Delta = 1.14, 1.17$, and 1.2 . When $U > U_{\text{cr}_2}$ new type of trajectories rise, such as the ones depicted by the dashed curves in the first panel of Figs. 15(a)–15(c), resulting in nonlinear bunching of the electron distribution function \tilde{f} [see second panel Figs. 15(a)–15(c)]. The amplitude of these p_x -nonlinear oscillations exceeds the size of the second Brillouin zone caused due to an anomalous Doppler shift and a normal Doppler shift near the end of the first and the second Brillouin zone respectively. As U changes between U_{cr_2} and U_{cr_3} , the nonlinear bunching becomes more prominent at the value of $2U/\Delta = 1.08$ [second panel Fig. 15(c)], coinciding with a local maximum of $v_m(U)$ in Fig. 4. This behavior implies a balanced mixture of anomalous and normal Doppler emissions similar to Smith-Purcell effects in photonics crystals [46]. Once U lies between U_{cr_3} and U_{cr_4} more complicated trajectories emerge involving three-phonon emissions, e.g., black dashed curve in the left panel of the Fig. 15(d). Finally, calculating the averaged electron energy and potential energy further confirms the absorption-emission events since the amplitude of their oscillations is enhanced with the variation of U , implying the emission (absorption) of larger number of phonons. Note $E_a(t)$ and $V_a(t)$ in third and fourth panel of Figs. 15(a)–15(f).

APPENDIX C: DERIVATION OF THE SOUND ABSORPTION COEFFICIENT

Consider a coherent acoustic wave that propagates through the superlattice. We want to study its evolution and the attenuations effects due to the interaction with the electrons and the crystal under the Hamiltonian Eq. (3). Then, the derivative of H with respect to time is given by

$$\dot{H} = \frac{\partial \mathcal{E}}{\partial p_x} \dot{p}_x + \frac{\partial V}{\partial x} \dot{x} + \frac{\partial H}{\partial t}. \quad (\text{C1})$$

By averaging Eq. (C1) over $T_s = 2\pi/\omega_s$, we obtain

$$\langle \dot{H} \rangle_{T_s} = 2k_s U \left\langle \left(\frac{v_x(p_x)}{v_0} - \frac{v_s}{2v_0} \right) \cos(k_s x - \omega_s t) \right\rangle_{T_s}. \quad (\text{C2})$$

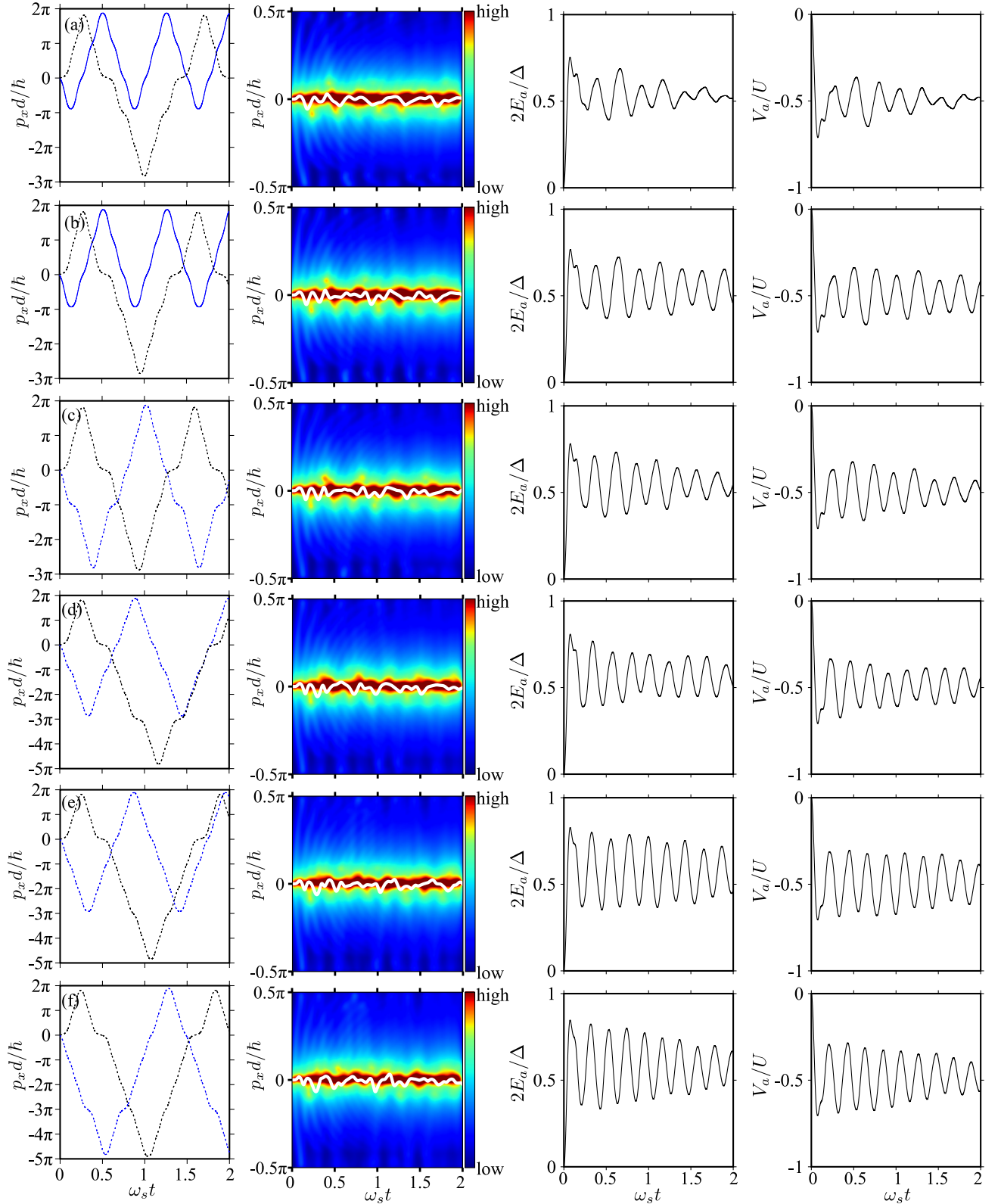


FIG. 15. The temporal dynamics of p_x -space trajectories subjected to normal and anomalous Doppler instabilities (first panel), the electron bunches (second panel), the averaged electron energy E_m (third panel) and the averaged potential energy V_m (fourth panel) for (a) $2U/\Delta = 1.06$, (b) $2U/\Delta = 1.08$, (c) $2U/\Delta = 1.1$ with $U_{c2} < U < U_{c3}$ and (d) $2U/\Delta = 1.14$, (e) $2U/\Delta = 1.17$, (f) $2U/\Delta = 1.2$ with $U_{c3} < U < U_{c4}$. The black and blue curves in the first panel were calculated for $x_i = -\pi/(2k_x)$ and $-2/k_x$, respectively. The white lines in the second panel indicate the center of electron distribution as a function of time. The calculations have been performed using the parameters of the SL structure with $v_e/v_s = 22$.

To calculate the absorption Γ coefficient, we need to substitute the right-hand side of Eq. (C2) in the definition Eq. (21). The last step requires the exact solution of Boltzmann equation in the general case by using the path-integral approach [Eq. (20)].

APPENDIX D: SMALL-SIGNAL GAIN IN THE QUASISTATIC LIMIT

Here we discuss how a parameter, effectively the product $(v_0/v_s) \times (\omega_s\tau)$, is important for the appearance of electron bunches with a negative drift but also whether it can influence the interaction of electrons with the electric probe field in the quasistatic limit. By employing again the formulation for the amplitude, $E_s = k_s U/e$, of an effective acoustoelectric field, we obtain a generalized condition for the onset of the successive bifurcations derived by Eq. (18) which reads

$$\left(\frac{E_s}{E_c}\right)_n = \alpha + (2n - 3) \left(\frac{v_s}{v_e}\right) \left(\frac{\Delta\hbar}{2\tau}\right) k_s d. \quad (\text{D1})$$

Then from the above equation, it follows that α can also determine the amplitude of the acoustoelectric field for which the electron localization [see Eq. (19)] takes place. In addition, the second term of Eq. (D1) depends on v_s/v_e with $v_e = 2v_0/\pi$, which controls the size of the active region [Eq. (12)], the scattering induced broadening \hbar/τ incorporated in Eq. (20) and the product $k_s d$ which is associated with propagation of the acoustic wave. To investigate all the former considerations, we calculated first the drift velocity v_d as a function of v_0/v_s and $\omega_s\tau$ at $U = U_{cr2}$ [Fig. 16(a)] where the negative drift velocity is possible. The upper-right blue area indicates values $(v_0/v_s, \omega_s\tau)$ that result in an enhancement of the backward drift due to the complex Bloch oscillations which are linked to the anomalous Doppler effect. In contrast, the dark red area designates the region with no reversal of drift velocity to negative values. As a next step, we calculate the absorption, $\sigma_r(\omega, U)$, of an ac probe field as a function of an arbitrary amplitude U , of the acoustic wave by resorting to an exact solution of the BTE. We assume that frequency of the acoustic wave is $\omega_s\tau = 0.1$ whereas the signal field frequency is much smaller than the inverse relaxation time ($\omega\tau \ll 0.1$). Figure 16(b) demonstrates how the absorption changes with the variation of U for different superlattice parameters and therefore different values of the parameter a . By increasing the wave amplitude, the incoherent absorption remains positive (yellow curve) for $v_0/v_s = 13$ ($a \sim 1.3$) even if U exceeds the critical value U_{cr1} . On the contrary, for a larger miniband width, $\Delta = 20$ meV ($a \sim 3.5$), gain is feasible (blue curve) if U reaches the values, where the sign of σ_r starts to be sensitive to the Doppler frequency shifts. Remarkably, gain exhibits an abrupt change and attains a maximum value close to $U = U_{cr2}$ similar to the characteristic changes in drift velocity (see Fig. 7). These effects imply a sensitive dependence of absorption on the sign of drift velocity and α parameter. It then follows that the true parameter that determines the mode of absorption of the probe field is α rather than just $\omega_s\tau$. This occurs because ω_s and k_s enter in the kinetic equations into a combination. Interestingly, for an even larger $\alpha \sim 5.5$, the $\sigma_r(\omega)$ dips anew to negative values when $U = U_{cr3}$ [green curve, Fig. 16(a)].

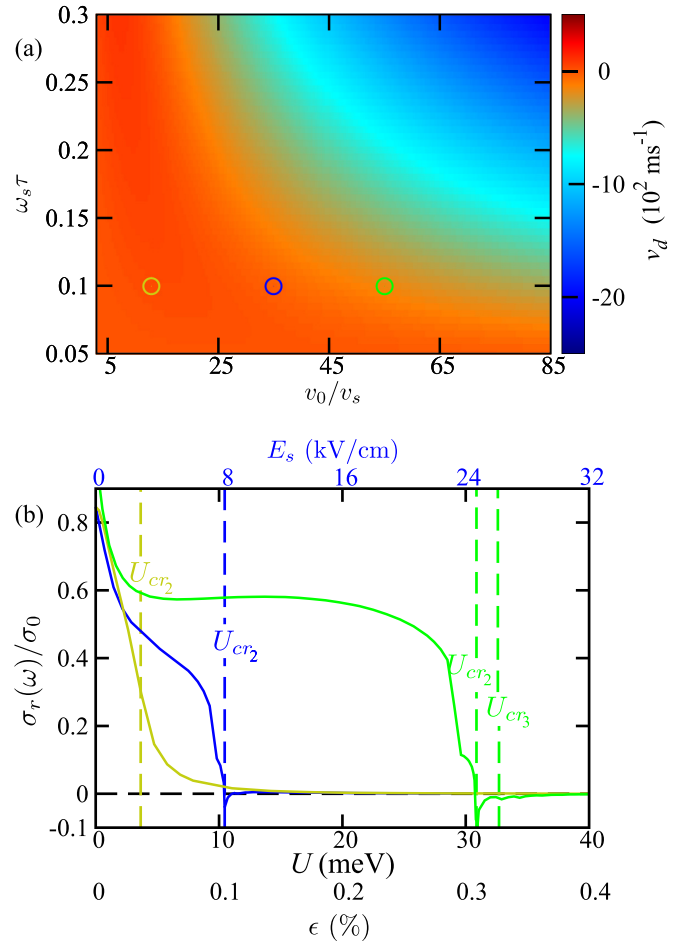


FIG. 16. (a) Color map showing the dependence of the drift velocity v_d on v_0/v_s and $\omega_s\tau$. The open circles mark the exact values of v_0 for which absorption was calculated numerically in the figure below. (b) Absorption $\sigma_r(\omega)$ of the oscillating field $E(t)$ as a function of the wave amplitude U (1st lower scale) or the strain magnitude ϵ (2nd lower scale) for $\omega\tau < 0.1$ and different values of $v_0/v_s = 13, 35, 55$. The upper scale denote the values of the acoustoelectric field [see Eq. (D1)] for a SL structure with $v_0/v_s = 35$ and $E_c = 2.3$ kV/cm. The vertical lines correspond to the $U = U_{cr2}$ for different SL parameters; see Table II.

APPENDIX E: KEY QUANTITIES AND PRACTICAL CONSIDERATIONS

In this Appendix, we provide further details regarding the superlattices structures considered to calculate the physical quantities related to acoustoelectric effects. Table II outlines the chosen parameters taken from realistic samples [16,38,73]

TABLE II. Parameters of superlattices studied.

Δ (meV)	d (nm)	τ (fs)	v_0/v_s	σ_0 (S/m)
miniband width	lattice period	scattering time	v_e/v_s	Drude conductivity
7	12.5	250	13 (10.5)	5.04
20	11.4	250	35 (22)	11.98
60	6	200	55 (35)	7.96

TABLE III. Critical values of the wave amplitude for the SL structures in Table II.

v_0/v_s	U_{cr1} meV	U_{cr2} meV	U_{cr3} meV	U_{cr4} meV
13	3.1	3.92	4.75	5.58
35	9.55	10.46	11.37	12.27
55	29.14	30.87	32.59	34.31

and depicts the critical ratio v_0/v_s that is largely responsible for the demonstration of different types of supersonic behavior and effectively controls the size of the active zone. A short overview of material properties, device design, experimental conditions and dominant scattering mechanisms determining τ in Table II can be found in Refs. [55,90–93]. The entries in the parentheses denote the ratio which is proportional to the effective electron speed ($v_e = 2v_0/\pi$) and it is involved in the expressions of the selections rules [Eq. (18)] allowing us to make a straight-forward comparison with their effects on direct transport in the quasiballistic limit. Furthermore, the fourth column gives the Drude conductivity which is used to scale the dynamical conductivity and therefore complementing Figs. 10 and 16.

One can characterize in a direct way the fraction of supersonic electrons by calculating the probability density $g(v(p_x))$ of miniband electron velocities for the particles starting from $x_i = 0$ and the initial momenta p_i uniformly distributed within the interval $(-\pi\hbar/d, \pi\hbar/d)$, i.e., within the first BZ. In this case, the miniband electron velocities obey a shifted arcsine distribution [94] whose probability density function is $g(v) = 1/(\pi\sqrt{(v_0)^2 - v^2})$ with $-v_0 < v(p_x) < v_0$. Figure 17 illustrates a colormap of g calculated versus $v(p_x)/v_s$ and v_0/v_s . For a typical SL structure with $v_0/v_s = 13$, whose parameters are given in Table II, the probability density g demonstrates values of small order ~ 0.01 in the subsonic (subluminal) region shown by the area between the dashed horizontal lines.

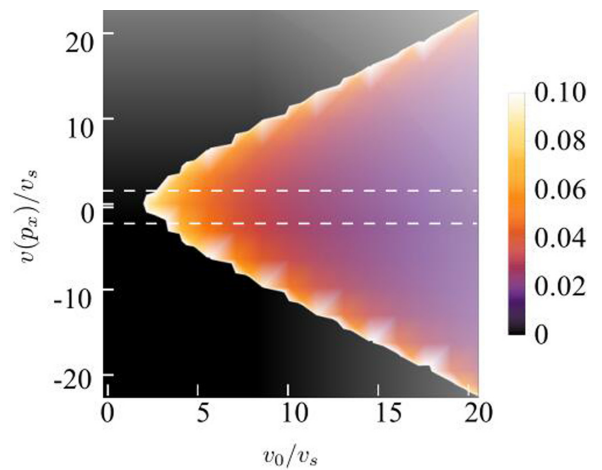


FIG. 17. Color map showing the probability density g of a particle's velocity $v(p_x)$ within $(-v_0, v_0)$ for p_x uniformly distributed over $(-\pi\hbar/d, \pi\hbar/d)$ and different ratios v_0/v_s .

Figure 17 reveals that g in the subsonic region is reduced significantly (transition between yellow and dark-purple colors) with the increase of v_0/v_s , ensuring that v would surpass v_s almost for any p_x at the limit $v_0 \gg v_s$.

Table III summarizes the critical values associated with the physical processes corresponding to bifurcations [cf. Eq. (9)]. The bolded entries represent the critical values of U which are all in excellent agreement with numerical simulations, as portrayed by Fig. 7. The wave amplitudes are directly proportional to the deformation potential D and the maximum strain, ϵ , that the acoustic wave creates. For the simulations in this work we consider $D = 10$ eV [38] and $\epsilon < 0.5\%$ which lies within an easily accessible experimental range [38,95]. These values are sufficiently large to reach the critical values of U described in Table II.

- [1] R. Hu, S. Iwamoto, L. Feng, S. Ju, S. Hu, M. Ohnishi, N. Nagai, K. Hirakawa, and J. Shiomi, Machine-Learning-Optimized Aperiodic Superlattice Minimizes Coherent Phonon Heat Conduction, *Phys. Rev. X* **10**, 021050 (2020).
- [2] J. Maire, R. Anufriev, R. Yanagisawa, A. Ramiere, S. Volz, and M. Nomura, Heat conduction tuning by wave nature of phonons, *Sci. Adv.* **3**, e1700027 (2017).
- [3] M.-H. Lu, L. Feng, and Y.-F. Chen, Phononic crystals and acoustic metamaterials, *Mater. Today* **12**, 34 (2009).
- [4] B. L. Davis and M. I. Hussein, Nanophononic Metamaterial: Thermal Conductivity Reduction by Local Resonance, *Phys. Rev. Lett.* **112**, 055505 (2014).
- [5] P.-A. Mante, Y.-R. Huang, S.-C. Yang, T.-M. Liu, A. A. Maznev, J.-K. Sheu, and C.-K. Sun, Thz acoustic phonon spectroscopy and nanoscopy by using piezoelectric semiconductor heterostructures, *Ultrasonics* **56**, 52 (2015).
- [6] G. Sitters, D. Kamsma, G. Thalhammer, M. Ritsch-Marte, E. J. Peterman, and G. J. Wuite, Acoustic force spectroscopy, *Nat. Meth.* **12**, 47 (2015).
- [7] J. D. Greener, A. V. Akimov, V. Gusev, Z. Kudrynskiy, P. H. Beton, Z. D. Kovalyuk, T. Taniguchi, K. Watanabe, A. Kent, and A. Patanè, Coherent acoustic phonons in van der waals nanolayers and heterostructures, *Phys. Rev. B* **98**, 075408 (2018).
- [8] M. Tamagnone, A. Ambrosio, K. Chaudhary, L. A. Jauregui, P. Kim, W. L. Wilson, and F. Capasso, Ultra-confined mid-infrared resonant phonon polaritons in van der waals nanostructures, *Sci. Adv.* **4**, eaat7189 (2018).
- [9] C. L. Poyser, L. H. Li, R. P. Champion, A. V. Akimov, E. H. Linfield, A. G. Davies, J. E. Cunningham, and A. J. Kent, A high electron mobility phonotransistor, *Commun. Phys.* **1**, 59 (2018).
- [10] T. I. Andersen, B. L. Dwyer, J. D. Sanchez-Yamagishi, J. F. Rodriguez-Nieva, K. Agarwal, K. Watanabe, T. Taniguchi, E. A. Demler, P. Kim, H. Park *et al.*, Electron-phonon instability in graphene revealed by global and local noise probes, *Science* **364**, 154 (2019).
- [11] A. Huynh, B. Perrin, N. D. Lanzillotti-Kimura, B. Jusserand, A. Fainstein, and A. Lemaître, Subterahertz monochromatic

- acoustic wave propagation using semiconductor superlattices as transducers, *Phys. Rev. B* **78**, 233302 (2008).
- [12] C. Poyser, A. Akimov, A. Balanov, R. Champion, and A. Kent, A weakly coupled semiconductor superlattice as a harmonic hypersonic-electrical transducer, *New J. Phys.* **17**, 083064 (2015).
- [13] T. E. Wilson, Evidence for terahertz acoustic phonon parametric oscillator based on acousto-optic degenerate four-wave mixing in a silicon doping superlattice, *Phys. Rev. B* **98**, 220304(R) (2018).
- [14] A. J. Kent, R. N. Kini, N. M. Stanton, M. Henini, B. A. Glavin, V. A. Kochelap, and T. L. Linnik, Acoustic Phonon Emission from a Weakly Coupled Superlattice under Vertical Electron Transport: Observation of Phonon Resonance, *Phys. Rev. Lett.* **96**, 215504 (2006).
- [15] F. Wang, C. L. Poyser, M. T. Greenaway, A. V. Akimov, R. P. Champion, A. J. Kent, T. M. Fromhold, and A. G. Balanov, Ultrafast Strain-Induced Charge Transport in Semiconductor Superlattices, *Phys. Rev. Appl.* **14**, 044037 (2020).
- [16] K. Shinokita, K. Reimann, M. Woerner, T. Elsaesser, R. Hey, and C. Flytzanis, Strong Amplification of Coherent Acoustic Phonons by Intraminiband Currents in a Semiconductor Superlattice, *Phys. Rev. Lett.* **116**, 075504 (2016).
- [17] I. Kaminer, S. E. Kooi, R. Shiloh, B. Zhen, Y. Shen, J. J. López, R. Remez, S. A. Skirlo, Y. Yang, J. D. Joannopoulos, A. Arie, and M. Soljačić, Spectrally and Spatially Resolved Smith-Purcell Radiation in Plasmonic Crystals with Short-Range Disorder, *Phys. Rev. X* **7**, 011003 (2017).
- [18] Y. Yang, A. Massuda, C. Roques-Carmes, S. E. Kooi, T. Christensen, S. G. Johnson, J. D. Joannopoulos, O. D. Miller, I. Kaminer, and M. Soljačić, Maximal spontaneous photon emission and energy loss from free electrons, *Nat. Phys.* **14**, 894 (2018).
- [19] C. Roques-Carmes, N. Rivera, J. D. Joannopoulos, M. Soljačić, and I. Kaminer, Nonperturbative Quantum Electrodynamics in the Cherenkov Effect, *Phys. Rev. X* **8**, 041013 (2018).
- [20] X. Shi, X. Lin, I. Kaminer, F. Gao, Z. Yang, J. D. Joannopoulos, M. Soljačić, and B. Zhang, Superlight inverse Doppler effect, *Nat. Phys.* **14**, 1001 (2018).
- [21] V. Ginzburg and I. Frank, On Doppler effect at superluminal velocity, *Doklady Acad. Nauk USSR* **56**, 583 (1947).
- [22] V. L. Ginzburg, Certain theoretical aspects of radiation due to superluminal motion in a medium, *Sov. Phys. Usp.* **2**, 874 (1960).
- [23] X. Lin and B. Zhang, Normal Doppler frequency shift in negative refractive-index systems, *Laser Photon. Rev.* **13**, 1900081 (2019).
- [24] M. T. Greenaway, A. G. Balanov, D. Fowler, A. J. Kent, and T. M. Fromhold, Using acoustic waves to induce high-frequency current oscillations in superlattices, *Phys. Rev. B* **81**, 235313 (2010).
- [25] A. Apostolakis, M. K. Awodele, K. N. Alekseev, F. V. Kusmartsev, and A. G. Balanov, Nonlinear dynamics and band transport in a superlattice driven by a plane wave, *Phys. Rev. E* **95**, 062203 (2017).
- [26] R. H. Parmenter, The acousto-electric effect, *Phys. Rev.* **89**, 990 (1953).
- [27] Y. V. Gulyaev, Acoustoelectronics (historical review), *Phys. Usp.* **48**, 847 (2005).
- [28] M. V. Nezlin, Negative-energy waves and the anomalous Doppler effect, *Sov. Phys. Usp.* **19**, 946 (1976).
- [29] I. E. Tamm, General characteristics of Vavilov-Cherenkov radiation, *Science* **131**, 206 (1960).
- [30] S. J. Smith and E. M. Purcell, Visible light from localized surface charges moving across a grating, *Phys. Rev.* **92**, 1069 (1953).
- [31] B. M. Bolotovskii and G. V. Voskresenskii, Emission from charged particles in periodic structures, *Sov. Phys. Usp.* **11**, 143 (1968).
- [32] K. N. Alekseev, E. H. Cannon, J. C. McKinney, F. V. Kusmartsev, and D. K. Campbell, Spontaneous dc Current Generation in a Resistively Shunted Semiconductor Superlattice Driven by a Terahertz Field, *Phys. Rev. Lett.* **80**, 2669 (1998).
- [33] B. J. Keay, S. Zeuner, S. J. Allen Jr, K. D. Maranowski, A. C. Gossard, U. Bhattacharya, and M. J. W. Rodwell, Dynamic Localization, Absolute Negative Conductance, and Stimulated, Multiphoton Emission in Sequential Resonant Tunneling Semiconductor Superlattices, *Phys. Rev. Lett.* **75**, 4102 (1995).
- [34] S. Kitorov, G. Simin, and V. Y. Sindalovskii, Bragg reflections and the high-frequency conductivity of an electronic solid-state plasma, *Sov. Phys. Solid State* **13**, 1872 (1972).
- [35] A. Ignatov and Y. A. Romanov, Nonlinear electromagnetic properties of semiconductors with a superlattice, *Physica Status Solidi (b)* **73**, 327 (1976).
- [36] R. F. Kazarinov and V. G. Skobov, On the theory of the amplification of ultrasound by semi-metals in electric and magnetic fields, *Sov. Phys. JETP* **16**, 1057 (1963).
- [37] L. Esaki and R. Tsu, Superlattice and negative differential conductivity in semiconductors, *IBM J. Res. Dev.* **14**, 61 (1970).
- [38] D. Fowler, A. Akimov, A. Balanov, M. Greenaway, M. Henini, T. Fromhold, and A. Kent, Semiconductor charge transport driven by a picosecond strain pulse, *Appl. Phys. Lett.* **92**, 232104 (2008).
- [39] Y. Galperin, S. Gantsevich, and V. Gurevich, Giant oscillations of sound absorption by metals in the case of open trajectories, *Sov. Phys. JETP* **29**, 926 (1969).
- [40] A. A. Abrikosov, *Fundamentals of the Theory of Metals* (Courier Dover Publications, New York, 2017).
- [41] J. Ashley, Phonon emission in piezoelectric solids, *J. Appl. Phys.* **36**, 528 (1965).
- [42] N. Rivera and I. Kaminer, Light-matter interactions with photonic quasiparticles, *Nat. Rev. Phys.* **2**, 538 (2020).
- [43] H. Chen and M. Chen, Flipping photons backward: reversed cherenkov radiation, *Mater. Today* **14**, 34 (2011).
- [44] V. L. Ginzburg and V. N. Tsytovich, *Transition Radiation and Transition Scattering* (Adam Hilger, Bristol, 1990).
- [45] M. Gintsburg, Anomalous Doppler effect in a plasma, *Sov. Phys. JETP* **14**, 542 (1962).
- [46] C. Luo, M. Ibanescu, S. G. Johnson, and J. Joannopoulos, Cherenkov radiation in photonic crystals, *Science* **299**, 368 (2003).
- [47] M. V. Kuzelev and A. A. Rukhadze, Stimulated radiation from high-current relativistic electron beams, *Sov. Phys. Usp.* **30**, 507 (1987).
- [48] A. D. Grigoriev, V. A. Ivanov, and S. I. Molokovsky, *Microwave Electronics* (Springer, New York, 2018), Vol. 61.
- [49] V. Narayanamurti, H. L. Störmer, M. A. Chin, A. C. Gossard, and W. Wiegmann, Selective Transmission of High-Frequency

- Phonons by a Superlattice: the “Dielectric” Phonon Filter, *Phys. Rev. Lett.* **43**, 2012 (1979).
- [50] S. Tamura, D. C. Hurley, and J. P. Wolfe, Acoustic-phonon propagation in superlattices, *Phys. Rev. B* **38**, 1427 (1988).
- [51] J. Isohätälä and K. N. Alekseev, Devil’s staircase, spontaneous dc bias, and chaos via quasiperiodic plasma oscillations in semiconductor superlattices, [arXiv:1201.6280](https://arxiv.org/abs/1201.6280).
- [52] K. V. Mardia and P. E. Jupp, *Directional Statistics* (Wiley, New York, 2000), Vol. 494.
- [53] H. Kroemer, On the nature of the negative-conductivity resonance in a superlattice bloch oscillator, [arXiv:cond-mat/0007482](https://arxiv.org/abs/cond-mat/0007482).
- [54] E. Schomburg, N. V. Demarina, and K. F. Renk, Amplification of a terahertz field in a semiconductor superlattice via phase-locked k-space bunches of bloch oscillating electrons, *Phys. Rev. B* **67**, 155302 (2003).
- [55] N. V. Demarina and K. F. Renk, Bloch gain for terahertz radiation in semiconductor superlattices of different miniband widths mediated by acoustic and optical phonons, *Phys. Rev. B* **71**, 035341 (2005).
- [56] H. N. Spector, Interaction of acoustic waves and conduction electrons, in *Solid State Physics* (Academic Press, New York, 1966), Vol. 19, pp. 291–361.
- [57] T. Fromhold, A. Patane, S. Bujkiewicz, P. Wilkinson, D. Fowler, D. Sherwood, S. Stapleton, A. Krokhin, L. Eaves, M. Henini *et al.*, Chaotic electron diffusion through stochastic webs enhances current flow in superlattices, *Nature (London)* **428**, 726 (2004).
- [58] C. Kittel and P. McEuen, *Introduction to Solid State Physics* (Wiley, New York, 2018).
- [59] B. K. Ridley, *Quantum Processes in Semiconductors* (Oxford University Press, New York, 1999).
- [60] R. Tsu, *Superlattice to Nanoelectronics* (Elsevier, Oxford, UK, 2005).
- [61] K. N. Alekseev, M. V. Gorkunov, N. V. Demarina, T. Hyart, N. V. Alexeeva, and A. V. Shorokhov, Suppressed absolute negative conductance and generation of high-frequency radiation in semiconductor superlattices, *Europhys. Lett.* **73**, 934 (2006).
- [62] A. E. Hramov, V. V. Makarov, A. A. Koronovskii, S. A. Kurkin, M. B. Gaifullin, N. V. Alexeeva, K. N. Alekseev, M. T. Greenaway, T. M. Fromhold, A. Patanè, F. V. Kusmartsev, V. A. Maksimenko, O. I. Moskalenko, and A. G. Balanov, Subterahertz Chaos Generation By Coupling a Superlattice to a Linear Resonator, *Phys. Rev. Lett.* **112**, 116603 (2014).
- [63] H. F. Budd, The generalized path variable method, *J. Phys. Soc. Jpn.* **18**, 142 (1963).
- [64] C. MacCallum, Kinetic integral solutions of the boltzmann equation, *Phys. Rev.* **132**, 930 (1963).
- [65] F. G. Bass, V. V. Zorchenko, and V. I. Shashora, Theory of galvanomagnetic and high-frequency phenomena in super-lattice semiconductors, *Sov. Phys. Semicond.* **15**, 263 (1981).
- [66] E. I. Blount, Ultrasonic attenuation by electrons in metals, *Phys. Rev.* **114**, 418 (1959).
- [67] Y. M. Gal’perin, V. Gurevich, and V. Kozub, Nonlinear effects in the propagation of high-frequency sound in normal conductors, *Phys. Usp.* **22**, 352 (1979).
- [68] A. Wacker, Semiconductor superlattices: a model system for nonlinear transport, *Phys. Rep.* **357**, 1 (2002).
- [69] E. Lax and F. L. Vernon Jr, Microwave Phonon-Assisted Tunneling in Superconductors, *Phys. Rev. Lett.* **14**, 256 (1965).
- [70] A. A. Ignatov, E. Schomburg, J. Grenzer, K. Renk, and E. Dodin, Thz-field induced nonlinear transport and dc voltage generation in a semiconductor superlattice due to bloch oscillations, *Z. Phys. B* **98**, 187 (1995).
- [71] H. T. Grahn, K. Von Klitzing, K. Ploog, and G. H. Döhler, Electrical transport in narrow-miniband semiconductor superlattices, *Phys. Rev. B* **43**, 12094 (1991).
- [72] K. F. Renk, B. I. Stahl, A. Rogl, T. Janzen, D. G. Pavel’ev, Y. I. Koshurinov, V. Ustinov, and A. Zhukov, Subterahertz Superlattice Parametric Oscillator, *Phys. Rev. Lett.* **95**, 126801 (2005).
- [73] T. Hyart, J. Mattas, and K. N. Alekseev, Model of the Influence of an External Magnetic Field on the Gain of Terahertz Radiation from Semiconductor Superlattices, *Phys. Rev. Lett.* **103**, 117401 (2009).
- [74] J. Blakemore, Semiconducting and other major properties of gallium arsenide, *J. Appl. Phys.* **53**, R123 (1982).
- [75] T. Hyart, K. N. Alekseev, and E. V. Thuneberg, Bloch gain in dc-ac-driven semiconductor superlattices in the absence of electric domains, *Phys. Rev. B* **77**, 165330 (2008).
- [76] A. Wacker, Gain in quantum cascade lasers and superlattices: A quantum transport theory, *Phys. Rev. B* **66**, 085326 (2002).
- [77] H. Eisele, L. Li, and E. H. Linfield, High-performance gaas/alas superlattice electronic devices in oscillators at frequencies 100–320 ghz, *Appl. Phys. Lett.* **112**, 172103 (2018).
- [78] M. F. Pereira, J. P. Zubelli, D. Winge, A. Wacker, A. S. Rodrigues, V. Anfertev, and V. Vaks, Theory and measurements of harmonic generation in semiconductor superlattices with applications in the 100 ghz to 1 thz range, *Phys. Rev. B* **96**, 045306 (2017).
- [79] D. Hayton, A. Khudchenko, D. Pavelyev, J. Hovenier, A. Baryshev, J. Gao, T.-Y. Kao, Q. Hu, J. Reno, and V. Vaks, Phase locking of a 3.4 thz third-order distributed feedback quantum cascade laser using a room-temperature superlattice harmonic mixer, *Appl. Phys. Lett.* **103**, 051115 (2013).
- [80] Z. Shao, Z. Yin, H. Song, W. Liu, X. Li, J. Zhu, K. Biermann, L. L. Bonilla, H. T. Grahn, and Y. Zhang, Fast Detection of a Weak Signal by a Stochastic Resonance Induced by a Coherence Resonance in an Excitable gaas/al 0.45 ga 0.55 As Superlattice, *Phys. Rev. Lett.* **121**, 086806 (2018).
- [81] A. Dunn, C. Poyser, P. Dean, A. Demić, A. Valavanis, D. Indjin, M. Salih, I. Kundu, L. Li, A. Akimov *et al.*, High-speed modulation of a terahertz quantum cascade laser by coherent acoustic phonon pulses, *Nat. Commun.* **11**, 835 (2020).
- [82] N. Opačak, S. D. Cin, J. Hillbrand, and B. Schwarz, Frequency Comb Generation by Bloch Gain Induced Giant Kerr Nonlinearity, *Phys. Rev. Lett.* **127**, 093902 (2021).
- [83] A. Patanè, D. Sherwood, L. Eaves, T. Fromhold, M. Henini, P. Main, and G. Hill, Tailoring the electronic properties of gaas/alas superlattices by inas layer insertions, *Appl. Phys. Lett.* **81**, 661 (2002).
- [84] A. Wacker, A.-P. Jauho, S. Rott, A. Markus, P. Binder, and G. H. Döhler, Inelastic Quantum Transport in Superlattices: Success and Failure of the Boltzmann Equation, *Phys. Rev. Lett.* **83**, 836 (1999).
- [85] J. Meyer, D. Arnold, C. Hoffman, and F. Bartoli, Anisotropic screening and ionized impurity scattering in semiconductor superlattices and multiple quantum wells, *J. Appl. Phys.* **74**, 6676 (1993).

- [86] M. T. Greenaway, A. G. Balanov, and T. M. Fromhold, Resonant control of cold-atom transport through two optical lattices with a constant relative speed, *Phys. Rev. A* **87**, 013411 (2013).
- [87] A. R. Kolovsky and G. Mantica, Driven harper model, *Phys. Rev. B* **86**, 054306 (2012).
- [88] G. Skadron and M. Jones, Properties of the vlasov phase in plasma turbulence theory, *Phys. Fluids* **17**, 500 (1974).
- [89] T. H. Dupree, A perturbation theory for strong plasma turbulence, *Phys. Fluids* **9**, 1773 (1966).
- [90] R. Ferreira and G. Bastard, Evaluation of some scattering times for electrons in unbiased and biased single-and multiple-quantum-well structures, *Phys. Rev. B* **40**, 1074 (1989).
- [91] N. Sawaki, On the reduction of the electron-lo phonon scattering in a semiconductor superlattice, *J. Phys. C* **19**, 4965 (1986).
- [92] B. Goutiers, F. Aristone, E. Ranz, and F. Mollot, Scattering mechanisms and warm electrons associated with vertical transport in gaas/alas superlattices, *Superlatt. Microstruct.* **17**, 135 (1995).
- [93] T. Unuma, N. Sekine, and K. Hirakawa, Dephasing of bloch oscillating electrons in gaas-based superlattices due to interface roughness scattering, *Appl. Phys. Lett.* **89**, 161913 (2006).
- [94] B. C. Arnold and R. A. Groeneveld, Some properties of the arcsine distribution, *J. Am. Stat. Assoc.* **75**, 173 (1980).
- [95] P. J. S. van Capel, E. Péronne, and J. I. Dijkhuis, Nonlinear ultrafast acoustics at the nano scale, *Ultrasonics* **56**, 36 (2015).
- [96] L. D. Landau, in *Collected Papers* (Gordon and Breach, New York, 1965), pp. 67–68.